Tropical Pacific baroclinic mode contribution and associated long waves for the 1994–1999 period from an assimilation experiment with altimetric data

Boris Dewitte,[1] Séréna Illig,[2] Laurent Parent,[3] Yves duPenhoat,[2] Lionel Gourdeau,[2] and Jacques Verron[3]

Received 26 February 2002; revised 12 December 2002; accepted 10 February 2003; published 18 April 2003.

[1] An Ocean General Circulation Model (OGCM) of the tropical Pacific in which combined TOPEX/Poseidon and ERS sea level anomalies are assimilated over January 1994 through July 1999, is used to investigate equatorial wave characteristics during the intense 1997–1999 El Niño-La Niña event. Near the equator, the linear vertical modes are estimated at each grid point of the OGCM simulation with and without assimilation. Consistently with an increase of the vertical gradient within the thermocline and a rise of the thermocline depth in the eastern basin, the assimilation results in an increased contribution of the higher-order baroclinic modes in the eastern basin and a decreased contribution of the first baroclinic mode in the western Pacific for the zonal current variability. For pressure, the first baroclinic mode contribution is reduced whereas the higher-order modes contribution is weakly impacted. Kelvin and first-meridional Rossby waves are then derived for the first two more energetic baroclinic modes in the simulation with assimilation. Kelvin waves of both modes constructively contribute to the strong warming observed in 1997, with the first (second) baroclinic mode being more energetic than the second (first) baroclinic mode in the early (mature) stage of the warming. Kelvin waves of both modes reflect as first meridional Rossby waves at the eastern boundary (reflection efficiency of ~95%) and contribute to push back the warm pool westward. The reversal of the warming is apparently initiated by the second baroclinic mode contribution which controls the position of the 28°C isotherm in the surface layer in the far eastern Pacific from January 1998. At the western boundary, reflections of Rossby waves take place for both modes with an estimated total efficiency of ~50% at 165°E. This suggests that, in our model, the delayed oscillator theory is not applicable for explaining the reversal from warm to cold conditions in 1998 while the zonal advective feedback was at work. More generally, the study suggests that it is necessary to take into account the vertical structure of the ocean when interpreting altimetric data, which can be done through an assimilation experiment. *INDEX TERMS:* 4215 Oceanography: General: Climate and interannual variability (3309); 4231 Oceanography: General: Equatorial oceanography; 4522 Oceanography: Physical: El Niño; 4504 Oceanography: Physical: Air/sea interactions (0312); *KEYWORDS:* El Niño, assimilation, Kelvin and Rossby waves, altimetry, boundary reflections

Citation: Dewitte, B., S. Illig, L. Parent, Y. duPenhoat, L. Gourdeau, and J. Verron, Tropical Pacific baroclinic mode contribution and associated long waves for the 1994–1999 period from an assimilation experiment with altimetric data, *J. Geophys. Res.*, *108*(C4), 3121, doi:10.1029/2002JC001362, 2003.

1. Introduction

[2] From recent modeling and observational studies, there is increasing evidence that the vertical structure of the low-frequency variability found in the tropical Pacific Ocean cannot be reduced to a single mode, i.e., the first baroclinic mode [*Kessler and McCreary*, 1993; *McPhaden*, 1999; *Dewitte and Reverdin*, 2000; *Shu and Clarke*, 2002]. From a forced Ocean General Circulation Model (OGCM) simulation, *Dewitte et al.* [1999] showed that the zonal current anomaly in the eastern Pacific is largely associated with the second baroclinic mode whereas the first baroclinic mode is dominant in the western Pacific. Higher-order modes also exhibit a relatively large variability in the eastern basin and are involved in the model dispersion process [cf. *Busalacchi and Cane*, 1988] induced by the sloping of the thermocline from west to east. *Delcroix et al.* [2000] and *Dewitte et al.* [2002] compared observations with multimode linear sim-

[1]Institut de Recherche pour le Développement/Laboratoire d'Etude en Géophysique et Océanographie Spatiale, Nouméa, New Caledonia.
[2]Laboratoire d'Etude en Géophysique et Océanographie Spatiale/Centre Nationale d'Etude Spatiale/Institut de Recherche pour le Développement, Toulouse, France.
[3]Laboratoire des Ecoulements Géophysique et Industriels, Grenoble, France.

0148-0227/03/2002JC001362

ulations and noted a much better agreement for sea level and zonal current anomalies derived from altimetry when more than one baroclinic mode is used. In particular, the amplitude in sea level anomaly along the equator during the strong 1997 El Niño as observed from the TOPEX/Poseidon data (hereinafter referred to as T/P data) is not recovered from a linear model without the second baroclinic contribution. In a coupled context, *Dewitte* [2000] and *Yeh et al.* [2001] showed that the ocean's vertical structure could also determine the timescales of the variability in sea surface temperature anomalies (hereinafter referred to as SSTAs) in the tropical Pacific. In their model, the relative contribution of the baroclinic modes (mostly mode 1 versus mode 2) controls the characteristics of the unstable coupled modes and therefore the duration and amplitude of the El Niño events.

[3] At the same time, with the development of observing systems, there has been considerable effort devoted to the design of assimilation techniques in order to improve the coherency between model and data and to "propagate" the precious information provided by the data over larger spatial and temporal windows. The success of these techniques varies depending on the underlying theories of the assimilation scheme, the data and the model that are used, and the region of investigation. The tropics, with a marked equatorial thermocline, present a highly linear physics, which may explain why the models are by themselves generally successful in simulating most features of the low-frequency (seasonal to interannual) variability when forced with realistic forcing. Therefore, in these regions where the variability associated with the equatorial waves is constrained by the structure and position of the thermocline, the assimilation scheme should help confine the isotherms at the correct position, which also means respecting to the vertical gradients.

[4] Thus, depending on the characteristics of the model and assimilation procedure, data assimilation may result in a drastic redistribution of the energy of the baroclinic modes and consequently in a change of the equatorial wave characteristics. The present paper focuses on an assimilation experiment using a technique which was recently shown to be successful in improving model simulations of the tropical Pacific [*Gourdeau et al.*, 2000; *Parent et al.*, 2002]. *Gourdeau et al.* [2000] showed that the assimilation of T/P data of 1993–1996 in the *Gent and Cane* [1989] model resulted in improving temperature vertical gradient, temperature variability within the thermocline and zonal current variability in the first 300 m. As shown by *Parent et al.* [2002], this assimilation method, named the SEEK filter (for Singular Evolutive Extended Kalman filter [cf. *Pham et al.*, 1998]), was applied to another OGCM of the tropical Pacific which has been widely used for El Niño Southern Oscillation (ENSO) studies [*Vialard and Delecluse*, 1998a, 1998b; *Vialard et al.*, 2001; *Radenac et al.*, 2001]. The period of assimilation (January 1994 through July 1999) now includes the 1997–1998 El Niño and the subsequent La Niña. Thus this experiment can be used to assess the "robustness" of SEEK and to assess the impact of the assimilation for an interannual event of large magnitude. From a more physical point of view, this experiment offers the opportunity to study the equatorial waves propagation and their reflection onto the meridional boundaries over this period. Recent studies have already investigated this issue. They, however, assume "one mode" for interpreting the T/P data [*Boulanger and Fu*, 1996; *Boulanger and Menkes*, 1999]. Although there are limitations linked to the use of non-biases-free model and assimilation scheme, our study offers an alternative method which may bring new insight for the analysis of altimetric data. In addition, the study aims at investigating the subsurface variability induced by higher-order baroclinic modes that are believed to be important for the generation and development of El Niño [*Dewitte et al.*, 2002].

[5] The paper is organized as follows. Section 2 presents the OGCM, the assimilation method, the data that were used for the assimilation, for the forcing of the model and for the intercomparison. Section 3 summarizes and complements former results on the comparison of the simulations (with and without assimilation) to independent observations in order to assess the impact of the assimilation on the fields that will constrain the equatorial wave characteristics. In section 4, a vertical mode decomposition of the OGCM is performed and the baroclinic mode contributions to pressure and current anomalies are studied. The sequence of the equatorial waves according to the more energetic baroclinic modes is then investigated for the 1997–1998 El Niño in section 5. Section 6 summarizes and provides a perspective for this work.

2. Model and Data

2.1. Model and Forcing

[6] A tropical version of the OPA Ocean General Circulation Model [*Madec et al.*, 1999] similar to the one used by *Vialard and Delecluse* [1998a, 1998b] is used in this study. We will briefly review its main characteristics here. The model is based on the standard hydrostatic primitive equations (including potential temperature, currents and salinity), solved by a finite difference scheme on a C grid. The domain covers the tropical Pacific from 120°E to 75°W, 30°N to 30°S, with realistic coastline and bathymetry. The zonal resolution is 1 degree, and the meridional resolution varies from 0.5 degrees in the equatorial waveguide to 2 degrees at the northern and southern boundaries. There are 25 vertical levels with a 10-m resolution at the surface down to 120 m. Lateral mixing is applied along horizontal surfaces, using a Laplacian operator. Vertical mixing is estimated from a turbulent kinetic energy closure prognostic equation [*Blanke and Delecluse*, 1993]. The reader is referred to *Vialard et al.* [2001] or *Parent* [2000] for further description of the model physics and configuration.

[7] The boundary conditions for the OGCM include surface fluxes of momentum, heat and salinity. Those are computed from a specified wind stress, net heat flux, and evaporation minus precipitation (no runoff). The surface fluxes of momentum results from a combination of ERS1-2 scatterometer derived wind stresses and Tropical Atmosphere Ocean (TAO) derived stresses [*Menkes et al.*, 1998]. The other surface boundary conditions come from the NCEP/NCAR reanalysis [*Kalnay et al.*, 1996]. The strong coupling between surface ocean heat loss and SST is approximated by a local restoring term toward observed sea surface temperature [*Reynolds and Smith*, 1994]. A constant correction is applied to the freshwater forcing. In

contrast with the surface heat flux feedback term, it has no physical grounds. It is a correction required to avoid sea surface salinity drift arising from errors in the prescribed freshwater budget and model imperfection.

2.2. Data

[8] In addition to the altimetric data that are assimilated, a variety of data sets were used for validating the assimilation experiment.

2.2.1. Altimetric Data

[9] The gridded sea level anomaly (SLA) data were supplied by AVISO/altimetry [*Ducet et al.*, 2000]. They were built by optimal interpolation of T/P and ERS data (hereinafter referred to as T/P + ERS data) on a 1/4° × 1/4° grid every 10 days. The SLAs are referenced to the first 3 years of the T/P mission. If the precision of individual instantaneous measurement is of the order of 6 cm RMS [*Fu et al.*, 1994], errors on such gridded data is estimated to 2–3 cm RMS for 10-day map and spatial scales of the order of 200 km and more [*Le Traon and Ogor*, 1998]. Gridded data are assimilated every 10 days.

2.2.2. TAO Data

[10] In situ temperature and current data from the TAO array [*Hayes et al.*, 1991; *McPhaden et al.*, 1998] were used in this study. Vertical profiles of zonal current and temperature data from equatorial TAO moorings at 147°E, 156°E, 165°E, 170°W, 140°W and 110°W were linearly interpolated on the vertical model grid. Dynamic height was computed using climatological salinity. Daily current and temperature data were averaged into 10-day bins for comparison with model outputs.

2.2.3. XBT

[11] The subsurface temperature measurements were provided by Neville Smith of the Bureau of Meteorological Research Center (BMRC) in Australia. The BMRC data set combines expandable bathythermograph data (XBT) with data from TAO array moorings using an optimal interpolation scheme to create a gridded data set with monthly values at every 1° of latitude (30°S–30°N) and 2° of longitude (100°E–70°W) at a set of 14 depths between the surface and 500 m [*Smith*, 1995].

2.3. Methodology

2.3.1. Assimilation Experiment

[12] The assimilation method used is sequential and based on the SEEK filter which is an extended reduced order Kalman filter. It was introduced by *Pham et al.* [1998] and validated by twin experiments in the tropical Pacific ocean by *Verron et al.* [1999]. With such an approach, as in similar approaches [e.g., *Cane et al.*, 1996; *Fukumori et al.*, 1999], the general idea is to reduce the enormous computing requirements by defining the error covariance matrix with a reduced number of degrees of freedom. The error subspace is represented by a limited number of three-dimensional, multivariate empirical orthogonal functions (EOFs) describing the dominant modes of the free-model variability. The SEEK filter was applied to the assimilation of the T/P + ERS data into the OPA model by *Parent et al.* [2002] in the same way as it was by *Gourdeau et al.* [2000]. For further description of the assimilation method, the reader is invited to refer to these papers.

[13] The assimilation experiment used here, described by *Parent et al.* [2002] as the ASS/SSH1 experiment, was performed over a 5-year period of the T/P mission from January 1994 to July 1999, starting from an initial state defined after a 1-year model run initialized with a "realistic" state in January 1993. Gridded sea level anomalies are assimilated every 10 days, and the output used from the assimilation experiments is the forecast state, also sampled every 10 days. The assimilation impact can be evaluated by comparison with the free model run and can also be quantified using independent in situ surface and subsurface data. In the following, the simulation without assimilation will be called CR (for Control Run) whereas the simulation with the assimilation of T/P + ERS data will be called ASSIM.

2.3.2. Analysis

[14] A "classical" comparison of the model outputs to the observations is first presented in order to assess the realism of the simulation and the impact of the assimilation of T/P + ERS data. Only a few aspects of the model variability and mean state will be stressed out here, knowing that most results concerning this experiment (description and validation) are given by *Parent* [2000] and *Parent et al.* [2002].

[15] The second step of the analysis focuses on the baroclinic mode contribution to sea level and zonal current anomalies. A decomposition in vertical modes of the model variables is thus sought at each longitude along the equator leading to the structure function $F_n(x, z)$. Zonal and meridional currents $\{u(x, y, z, t)\}$ and pressure $\{p(x, y, z, t)\}$ anomalies are estimated relative to the climatological seasonal cycle of the 1994–1996 simulation (3 years). These fields are then projected on the vertical structure functions $F_n(x, z)$. This implies computing the following quantity: $\langle q(x, y, z, t)|F_n(x, z)\rangle = \int_{H(x)}^{0} q(x, y, z, t)\, F_n(x, z)dz$, $H(x)$ being the ocean depth, and q being u or p. The method is detailed by *Dewitte et al.* [1999].

3. Comparison to the Observations

[16] In the work of *Gourdeau et al.* [2000], 4 years of T/P sea level anomalies (1993–1996) were assimilated into a reduced gravity ocean model, and it was found that the assimilation of altimeter data was useful to control the subsurface thermal and velocity structures. In the OPA model, the impact of T/P + ERS data is also noticeable, although much weaker due to the good skill of the "free" model in simulating the low frequency variability in the tropical Pacific. *Vialard et al.* [2001] used the same OPA model and forcing (except that there is no flux correction) and compared the model outputs to a variety of observations (T/P data, TAO data and the *Reynolds and Smith* [1994] SST data) for the 1993–1998 period. The model was shown to reproduce the main features of the tropical Pacific mean state, despite a weaker than observed thermal stratification, a slightly too strong (weak) south equatorial current (north equatorial countercurrent), and a slight underestimation of the equatorial undercurrent. A very good agreement was found between the model dynamic height and T/P sea level variability, with correlation/rms difference of 0.80/4.7 cm on average in the 10°S–10°N band. The model also compares quite well with the TAO current variability at the equator, with correlation/rms difference of 0.81/0.23 m s^{-1} for surface currents. Despite this high model perform-

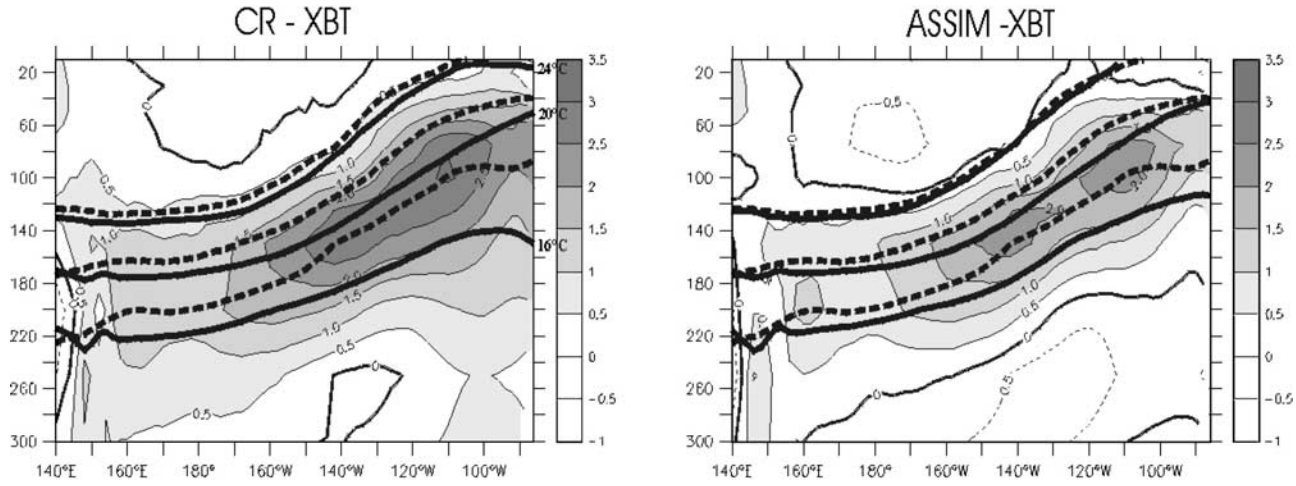

Figure 1. Equatorial mean temperature (January 1994–December 1998) difference in the first 300 meters (a) between CR (i.e., model simulation without assimilation of altimetric data) and the observations derived from XBT measurements and (b) between ASSIM (i.e., model simulation with assimilation of altimetric data) and the XBT observations. Unit is °C and shading is for values larger than 0.5°C. The mean isotherms 16°C, 20°C and 24°C are represented by solid lines for the OGCM outputs and by dashed lines for the observations.

ance without assimilation [*Vialard et al.*, 2001], *Parent et al.* [2002] showed that the assimilation of T/P + ERS data still allows reducing the misfit between observations and model counterparts in the equatorial band (10°S–10°N), especially with regard to the bias of the thermocline, in terms of location and structure. The zonal circulation along the equator is also better simulated, with a more realistic south equatorial current and equatorial undercurrent.

[17] In the following, we discuss some features of the model mean structure and interannual variability, which strongly constrain the equatorial waves dynamics, namely the mean temperature vertical structure along the equator that controls the structure of the baroclinic modes, and the interannual variability of dynamic height, temperature and zonal currents in the equatorial band. This section should be used as material for complementing the analysis of the impact of the assimilation onto the baroclinic mode contributions to sea level and zonal currents anomalies (section 4.3).

3.1. Mean Temperature Along the Equator

[18] Figure 1 shows the impact of the assimilation on the average temperature (January 1994 through July 1999) at the equator, based on a comparison with XBT data. The main discrepancy is found within the thermocline and consists on an average cooling. In the eastern part of the ocean, the assimilation results in a stronger cooling, with a maximum difference of 1.2°C near 200 m. It reduces the discrepancies between model and observations by almost 1°C. The assimilation run slightly improves the thermocline that is less diffuse than without the assimilation (identified as the thickness of the layer between the 16°C and 24°C isotherms). The improvement is particularly noticeable in the eastern part of the ocean, although the thermocline is still too diffuse compared to XBT and TAO data, which is a flaw in most OGCM simulations [*Vialard et al.*, 2001]. Moreover, the assimilation results in a shallower thermocline (identified by the depth of the isotherm 20°C), by up to 10 m shallower in the eastern part of the basin, which represents about 45% of the difference between observations and model without assimilation.

3.2. Interannual Variability

3.2.1. Sea Level and Dynamic Height

[19] Figure 2 presents variability maps of sea level anomalies for T/P, CR and ASSIM. As mentioned above, the model without assimilation (Figure 2b) is already successful in reproducing the sea level variability within 15°S–15°N with a high performance in the equatorial band (5°S–5°N) (see *Vialard et al.* [2001] for more details). Note, however, that the meridional scale of the variability varies less zonally in CR than in T/P. In T/P, it decreases eastward from 130°W, whereas it is almost constant for CR. This suggests an inaccurate representation of the zonal and vertical gradients of the thermal structure as discussed in section 4 that affects the characteristics of the Kelvin waves (phase speed and amplitude according to the baroclinic modes) in the central and eastern Pacific. The amplitude at ~7°N in the western and central part of the basin is also overestimated in CR. The assimilation reduces these discrepancies (Figure 2c).

[20] A comparison of the model dynamic height (HDYN) and 20°C isotherm (D20) anomalies to the TAO data confirms the improvement brought by the assimilation (Figure 3). For HDYN anomalies, the RMS difference (RMSD) is reduced by 4 cm on average, over the basin, whereas for D20 anomalies, RMSD decreases from 23 m for CR to 16 m for ASSIM on average with the largest impact near 6°N–8°N and in the upwelling region (110°W; 0°–8°S). The best agreement between observations and ASSIM is found in the equatorial band: For HDYN, correlation is larger than 0.9 and RMSD is of the order of 3 cm.

3.2.2. Zonal Current Along the Equator

[21] The comparison is done with TAO currentmeter moorings situated along the equator. Table 1 shows the results at five locations along the equator. Zonal currents from both CR and ASSIM are overall in good agreement with observations with correlations usually larger than 0.5.

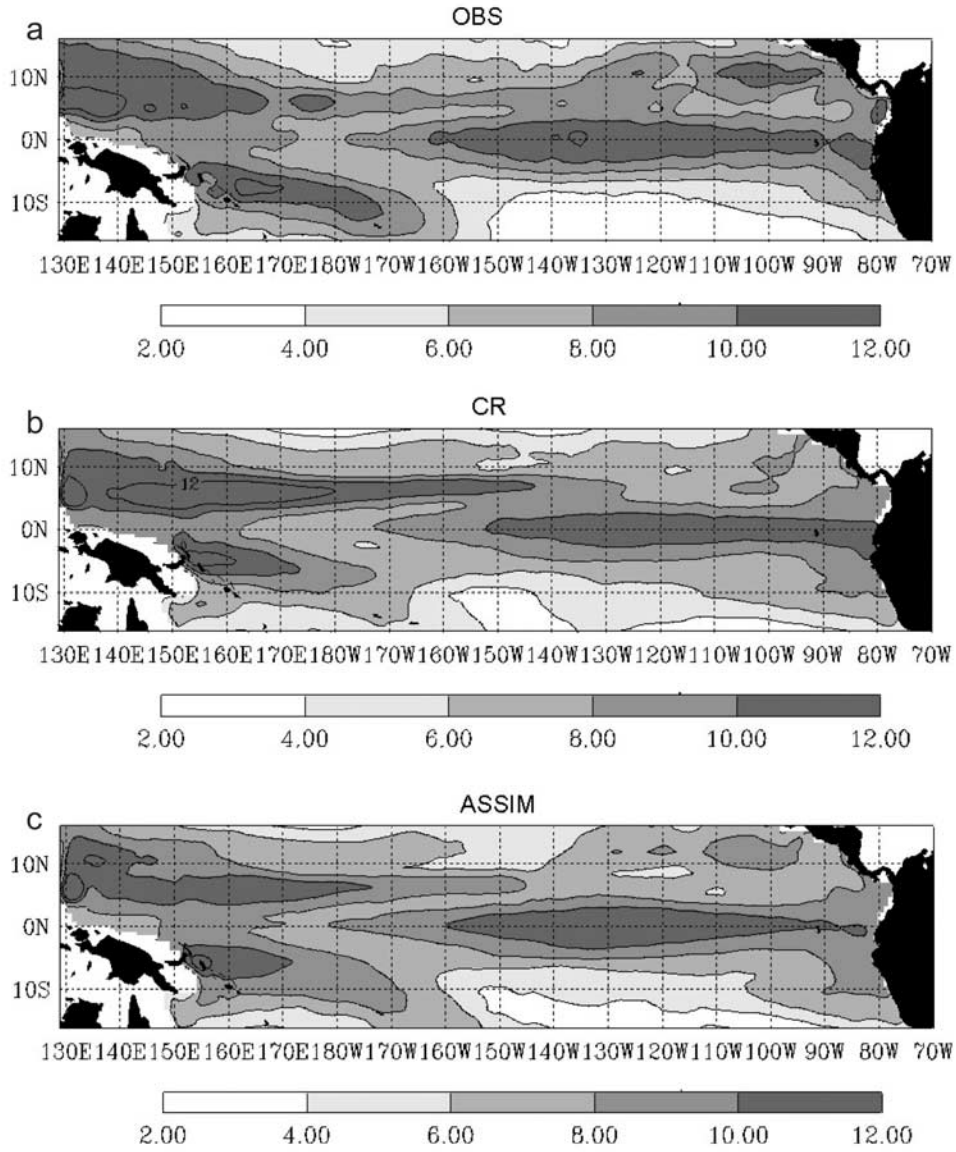

Figure 2. Variability (rms) maps of sea level anomalies (January 1994–December 98) for (a) observations (T/P + ERS), (b) CR and (c) ASSIM. Units are centimeters [after *Parent et al.*, 2002].

In the central and eastern Pacific, the model reproduces the westward flowing South Equatorial Current (SEC) at the surface, and the eastward flowing Equatorial Under Current (EUC) beneath. In the western Pacific, even the subtle layered structure of the flow, with slight eastward flow at the surface (156°E, 165°E), westward flow beneath, and the eastward EUC at 150 m and deeper is well reproduced [see also *Vialard et al.*, 2001]. The improvement brought by the assimilation is noticeable in the central and eastern Pacific since it happens within the thermocline, with both an increase of the correlation and a reduction of RMSD. This, in particular, results in a better representation of the EUC variability which was systematically underestimated in CR (by 10 to 20 cm s^{-1}). It is worth pointing out that the currents at 170°W are improved down to 131 m, although the agreement between observation and CR was already very good at this location. The assimilation however does not systematically lead to improvements. In particular, at 147°W and 165°W and below the thermocline at 110°W, correlation is generally reduced by ~0.1 (~0.25) above (below) 100 m with also larger RMSD.

[22] Although the assimilated fields do have the better consistency with the altimetric data and consequently are still of better interest for the present study, these flaws should be kept in mind when interpreting the results of the vertical mode decomposition.

4. Baroclinic Mode Contribution

[23] In this section, we focus on the variability characteristics of the baroclinic modes for ASSIM. The impact of the assimilation on these characteristics is also discussed.

4.1. Zonal Current Anomalies (ZCAs)

[24] Because the vertical functions for the gravest modes have no structure in the top 40 m, the projections of the

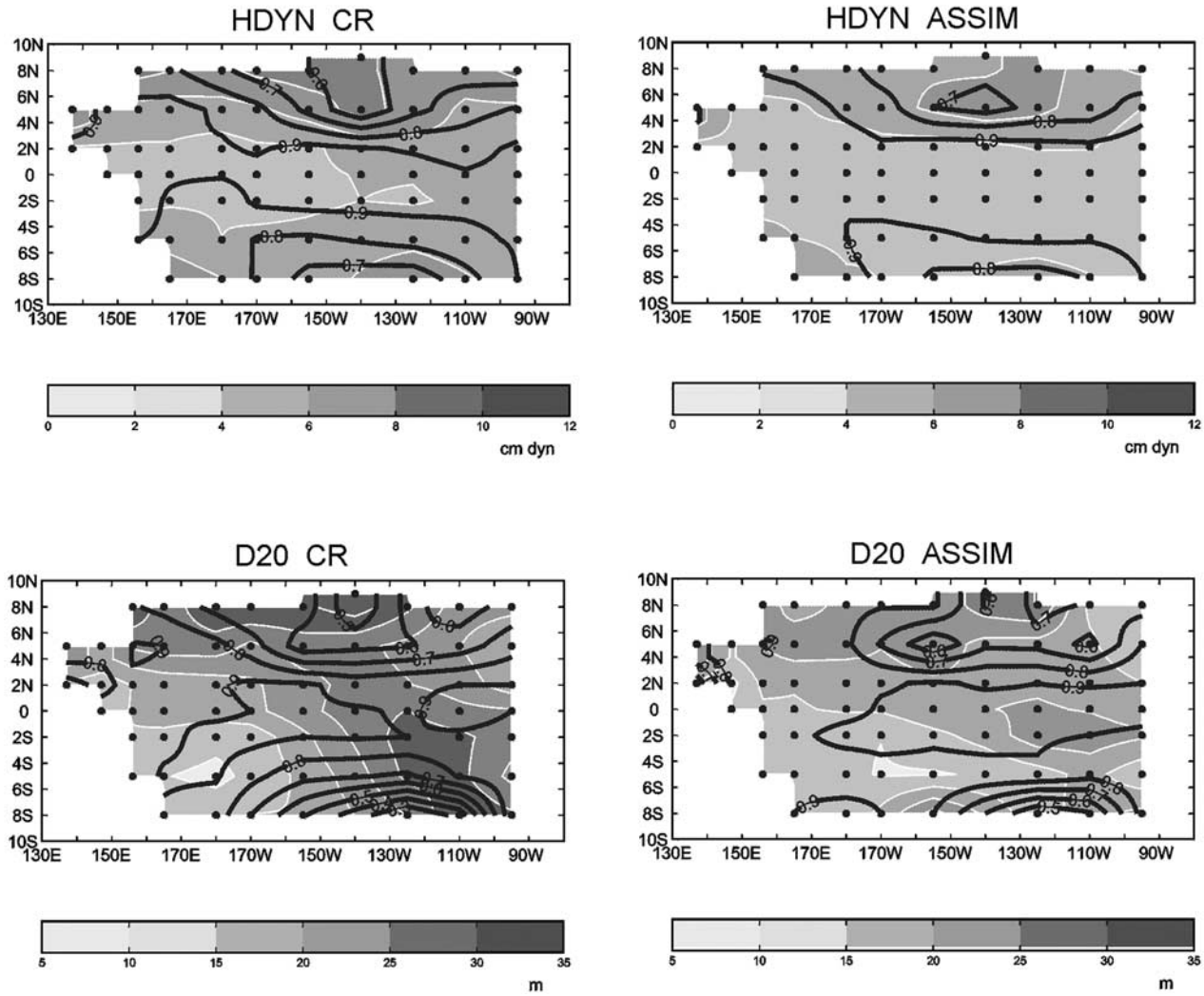

Figure 3. Rms difference (shading) and correlation (contours) between model ((left) CR and (right) ASSIM) and observations from the TAO moorings for the (top) dynamic height and (bottom) 20°C isotherm depth anomalies. Units are centimeters for dynamic height and meters for the 20°C isotherm depth.

current anomalies onto these modes also have no shear in the upper layer. Therefore, the surface zonal currents are estimated as the currents averaged over the four uppermost levels of the model (5 m to 35 m depth). This averaging removes part of the shear within the weakly stratified surface layer associated with incomplete mixing which cannot be represented in the vertical mode decomposition. The RMS (root mean square) variability of surface zonal current anomalies for the January 1994 through June 1999 period is presented in Figure 4a. Large values (>20 cm s^{-1}) are confined within 5°N–5°S, with maximum variability centered near the dateline. The zone of maximum variability is slightly north of the equator.

[25] Figures 4b and 4c illustrate the contribution of the first two gravest modes to these surface currents. Their RMS variability near the equator is much weaker than the total RMS (Figure 4a). For mode 1, large values extend meridionally to 7°N–7°S, whereas variability of mode 2 is more confined near the equator. Mode 1 has a peak (23 cm s^{-1}) in the western Pacific, and mode 2 presents maxima of a larger magnitude (31 cm s^{-1}) in the eastern Pacific. In the central Pacific the contribution of the two modes have similar magnitudes. The two gravest modes explain 25% (correlation coefficient c = 0.68) of the total surface current variance over NINO4eq (150°W–160°E; EQ) and 37% (c = 0.80) over NINO3eq (90°W–150°W; EQ).

[26] The variability of the higher-order baroclinic modes is represented in Figure 4d (sum of mode 3 to 10). As expected, it is much more confined toward the equator compared to mode 1 and 2, with two peaks: one in the central Pacific corresponding to the region of the largest variability in the zonal wind anomalies (not shown), the other in the far eastern Pacific from 120°W corresponding to the abrupt change in the stratification as a function of longitude. The latter induces modal dispersion leading to a scattering of the energy from the gravest modes to the higher-order modes [see *Dewitte et al.*, 1999]. Over NINO4eq, the summed up contribution of mode 3 to 10 accounts for 33% of the explained variance of the total surface current anomalies, whereas over NINO3eq, explained variance is not significant.

[27] Figure 5 displays the time-evolution along the equator of the total surface current anomalies and its baroclinic

Table 1. Correlation and Root Mean Square (rms) Difference as a Function of Depth for Zonal Currents Anomalies Between the TAO Array Observations and the Simulations Without and With Assimilation Along the Equator[a]

	147°E TAO Mooring Jan. 1995–Dec. 1997		165°E TAO Mooring May 1995–Feb. 1997		170°W TAO Mooring Jan. 1994–June 1999		140°W TAO Mooring Sep. 1996–June 1999		110°W TAO Mooring June 1994–June 1999	
	Without	With	Without	With	Without	With	Without	With	Without	With
Correlation at 35 m	0.914	0.795	**0.907**	**0.934**	0.871	0.829	**0.847**	**0.904**	**0.797**	**0.839**
Correlation at 45 m	0.852	0.745	**0.892**	**0.910**	0.803	0.782	**0.832**	**0.913**	**0.837**	**0.868**
Correlation at 55 m	0.705	0.653	**0.870**	**0.885**	0.706	0.703	**0.826**	**0.891**	**0.840**	**0.866**
Correlation at 65.1 m	**0.562**	**0.642**	0.820	0.786	**0.611**	**0.674**	**0.812**	**0.875**	0.851	0.822
Correlation at 75.2 m	**0.481**	**0.633**	0.807	0.695	**0.595**	**0.694**	**0.865**	**0.885**	0.836	0.756
Correlation at 85.4 m	**0.448**	**0.534**	0.841	0.651	**0.644**	**0.738**	0.892	0.883	0.841	0.662
Correlation at 95.8 m	0.479	0.369	0.847	0.656	**0.744**	**0.810**	0.917	0.874	0.861	0.628
Correlation at 106.6 m	0.589	0.370	0.802	0.652	**0.829**	**0.872**	0.924	0.842	0.858	0.630
Correlation at 118.1 m	0.645	0.270	0.761	0.632	**0.859**	**0.883**	0.930	0.804	0.851	0.652
Correlation at 131.1 m	0.667	0.346	0.740	0.642	**0.852**	**0.866**	0.917	0.783	0.850	0.671
Correlation at 146.8 m	0.497	0.081	0.734	0.704	0.840	0.832	0.875	0.757	0.849	0.661
Correlation at 168 m	−0.110	−0.638	**0.737**	**0.794**	0.787	0.693	0.834	0.698	0.820	0.552
Correlation at 200 m	−0.183	−0.213	0.650	0.547	0.640	0.488	0.862	0.763	0.709	0.358
RMS difference (cm/s) at 35 m,	8.79	13.19	**19.80**	**12.46**	**16.91**	**16.64**	**16.72**	**14.67**	**18.32**	**16.79**
RMS difference (cm/s) 45 m	10.59	13.51	**16.12**	**11.67**	**18.35**	**16.79**	**16.87**	**15.37**	**16.92**	**16.67**
RMS difference (cm/s) 55 m	13.55	14.56	**14.76**	**11.72**	**19.62**	**18.20**	**17.04**	**16.16**	16.90	17.85
RMS difference (cm/s) 65.1 m	**15.38**	**14.13**	14.55	14.89	**21.49**	**18.91**	**17.33**	**15.94**	15.47	20.29
RMS difference (cm/s) 75.2 m	**15.69**	**13.45**	14.48	17.75	**22.16**	**19.16**	**15.06**	**14.65**	14.66	22.48
RMS difference (cm/s) 85.4 m	**16.06**	**14.95**	15.24	20.41	**22.08**	**19.26**	13.68	14.55	13.68	24.32
RMS difference (cm/s) 95.8 m	18.15	19.41	16.62	21.77	**20.59**	**18.06**	12.39	15.22	13.01	24.28
RMS difference (cm/s) 106.6 m	19.45	22.36	17.86	22.30	**18.35**	**15.89**	12.19	17.33	13.32	23.41
RMS difference (cm/s) 118.1 m	16.68	19.83	18.79	23.07	**16.29**	**15.37**	12.07	19.17	13.42	21.70
RMS difference (cm/s) 131.1 m	11.26	13.88	19.12	22.69	15.41	16.77	13.32	18.51	12.74	19.66
RMS difference (cm/s) 146.8 m	8.97	11.03	17.94	19.28	15.36	19.38	15.39	17.14	11.39	17.32
RMS difference (cm/s) 168 m	10.57	12.87	**13.44**	**11.64**	13.66	19.53	**16.00**	**15.62**	10.18	15.74
RMS difference (cm/s) 200 m	8.09	9.03	10.79	12.01	12.92	18.02	**12.34**	**11.15**	10.42	14.86

[a]Bold entries indicate where the assimilation reduces the model-data misfit (i.e., increased correlation and reduced RMS difference).

mode contributions. The characteristics identified in the RMS maps described above can be recognized with a larger variability for mode 1 (2) in the western (eastern) Pacific than in the eastern (western) Pacific. Strong eastward current anomalies in the western Pacific can be seen in the second half of 1997. They are associated with the second baroclinic mode contribution and the summed-up contribution of the high-order modes, whereas mode 1 exhibits westward anomalous currents during this period in the central Pacific. The reversal of the current from eastward to westward starts in January 1998. The mode 2 contribution is then very large due to downwelling Kelvin wave reflection at the eastern boundary (see section 5). The abrupt shift of the El Niño into La Niña in early 1998 [*Picaut et al.*, 2001] is apparently associated with the strong westward anomalous currents of the second baroclinic mode contribution.

4.2. Sea Level Anomalies (SLAs)

[28] Figure 6a presents time-longitude plots along the equator of the total SLAs. The contribution of the first two modes and of modes 3 to 10 is also presented (Figures 6b–6d). Because first-meridional Rossby waves yield a weak contribution to sea level variability along the equator, Figures 6b–6d provide an estimation of the Kelvin wave contribution. Clear propagations are noticeable across the whole basin for mode 1 with a phase speed value of 2.93 m s^{-1} at 180°, close to theory (phase speed value is estimated from the slope of maximum lag correlation between the time series at 180° and the points around). For mode 2 and the summed-up contribution of mode 3 to 10, the eastward propagation appears only east of the dateline. West of the date line, the sea level anomaly variability along the equator is much weaker than for mode 1. In the central and eastern Pacific, the baroclinic mode contributions are of the same order of magnitude. Mode 2 amplitude is however about twice that of mode 1 during 1997, and mode 3 contribution is as large as mode 1 contribution during this period. The percentage of explained variance is twice as large for mode 2 (∼40%) as for mode 1 in the eastern basin. It is much larger (6 times) for mode 1 than for mode 2 west of the dateline where it reaches 60% for mode 1. The percentage of explained variance for the summed-up contribution of mode

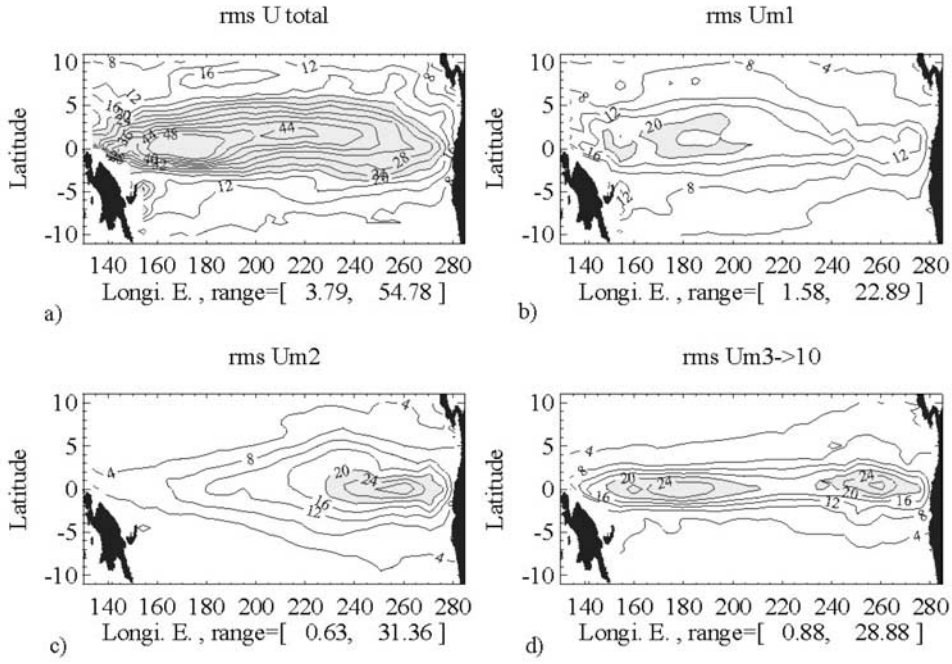

Figure 4. Maps of variability (rms) of (a) the ASSIM surface currents estimated as the average of the four top model levels, the contributions (b) of the first baroclinic mode, (c) of the second baroclinic mode and (d) of the sum of contributions of the third to the tenth mode. Units are cm s^{-1} and contour intervals are 4 cm s^{-1}.

3 to 10 is as large as mode 2 in the western and central Pacific (∼15%) and as mode 1 in the eastern Pacific.

4.3. Impact of the Assimilation

[29] As seen previously, the assimilation impacts the mean structure and the interannual variability. Changes in the mean structure impact the vertical mode structures. The impact is the largest for the high-order modes. The first baroclinic mode function is hardly modified. The largest changes for mode 2 and 3 are found in the western and the eastern part of the basin (not shown) where the assimilation changes the most the depth of the isotherms (see section 2). On top of these differences in the vertical functions are to be added the differences in the interannual variability between ASSIM and CR, in order to fully estimate the impact of the assimilation. Figures 7 and 8 display the maps of RMSD between ASSIM and CR for ZCAs and SLAs and their corresponding baroclinic mode contributions. For ZCAs, the assimilation amplifies the contribution of the high-order modes in the eastern Pacific and reduces the contribution of the gravest mode in the western Pacific. For sea level, the assimilation impacts mostly the first baroclinic mode contribution with a reduction of the variability in the western Pacific near 5°N and in the central-eastern equatorial Pacific. The variability of modes 2 and the summed-up contribution of modes 3 to 10 is affected to a lesser extent. Section 6 discusses further what is brought by the assimilation in terms of physics and interpretation of the waves sequence and their impact on SST.

5. Equatorial Waves and Boundary Reflections

[30] *Boulanger and Menkes* [1999] analyzed the wave sequence during the onset, growth and weakening of the 1997–1998 El Niño using T/P data. They discussed the relevance of the delayed action oscillator [*Schopf and Suarez*, 1988] and zonal advection [*Picaut et al.*, 1997] feedbacks for this period based on their estimation of the wave coefficient and the resulting reflection efficiency at the meridional boundaries. They conclude that, during the 1997–1998 El Niño, an important mechanism that leads to the reversal of the warm conditions in early 1998 was the delayed action oscillator and that the reflection efficiency (defined, at the western (eastern) boundary, as the percentage of the incoming Rossby (Kelvin) wave amplitudes actually reflecting) is ∼75% and ∼100% of that of an infinite meridional wall respectively at the eastern and western boundaries. The recent study by *Picaut et al.* [2002] complements the later study from the analysis of all the available satellite data during this period and discusses the relevance of the existing ENSO theories. They showed that, in addition to the recharge/discharge mechanism [*Jin*, 1997], both the delayed action oscillator and the zonal advective feedbacks were at work at various stages of the event, pointing out the necessity to better understand the transition from one mechanism to the other and their relative weight when acting together constructively on SST changes.

[31] In the following section, we complement their analysis in light of the results of the vertical mode decomposition. Although the simulation covers a longer period, we focus on the 1996–1998 period for clarity, but the estimation of the reflection efficiency at the meridional boundaries is based on the data that cover the whole period.

[32] To derive the coefficient for the meridional modes, both the sea level and zonal current baroclinic contributions are projected onto the complete basis of the long-

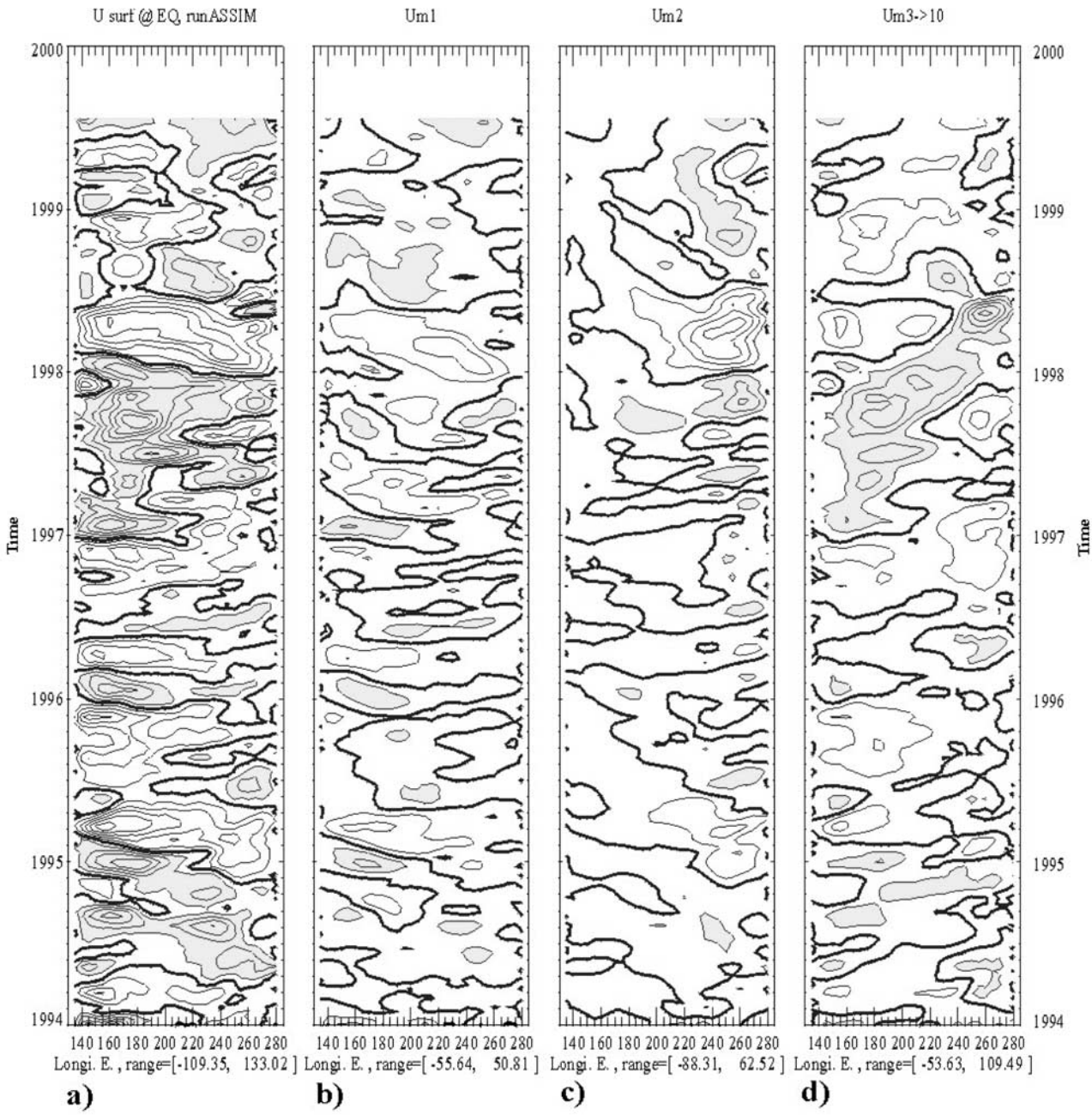

Figure 5. Time-longitude plots of (a) surface zonal current anomalies (ZCA) along the equator, and the contribution of (b) the first baroclinic mode, (c) the second one, and (d) the summed-up contribution of modes 3 to 10 from January 1994 until July 1999. Units are cm s^{-1} and contour intervals are every 20 cm s^{-1}. Shading is for anomalies larger than 20 cm s^{-1}. A three-grid-point running mean filter was applied in longitude and time for retrieving the small-scale features and easing the interpretation.

wavelength meridional modes. These are computed from the zonally varying phase speed derived from the vertical mode decomposition (section 4). The projection is performed between 10°S and 10°N. The method is similar to the one given by *Dewitte et al.* [1999]. For simplicity, only the results for the first two baroclinic modes are presented. However, although more dissipative, mode three will be also discussed because its contribution can be large at particular periods of time. The higher-order baroclinic modes are much less energetic than the first three modes and do not exhibit propagating features. It was checked that the first-meridional Rossby and Kelvin waves of the first three baroclinic modes explained at least 80% of the total SLA variance in the 5°S–5°N band so that emphasis will be made on these two meridional modes.

5.1. Waves Sequence for the 1996–1998 Period

[33] Figures 9 and 10 display the Kelvin and first meridional Rossby contributions to SLAs along the equator for

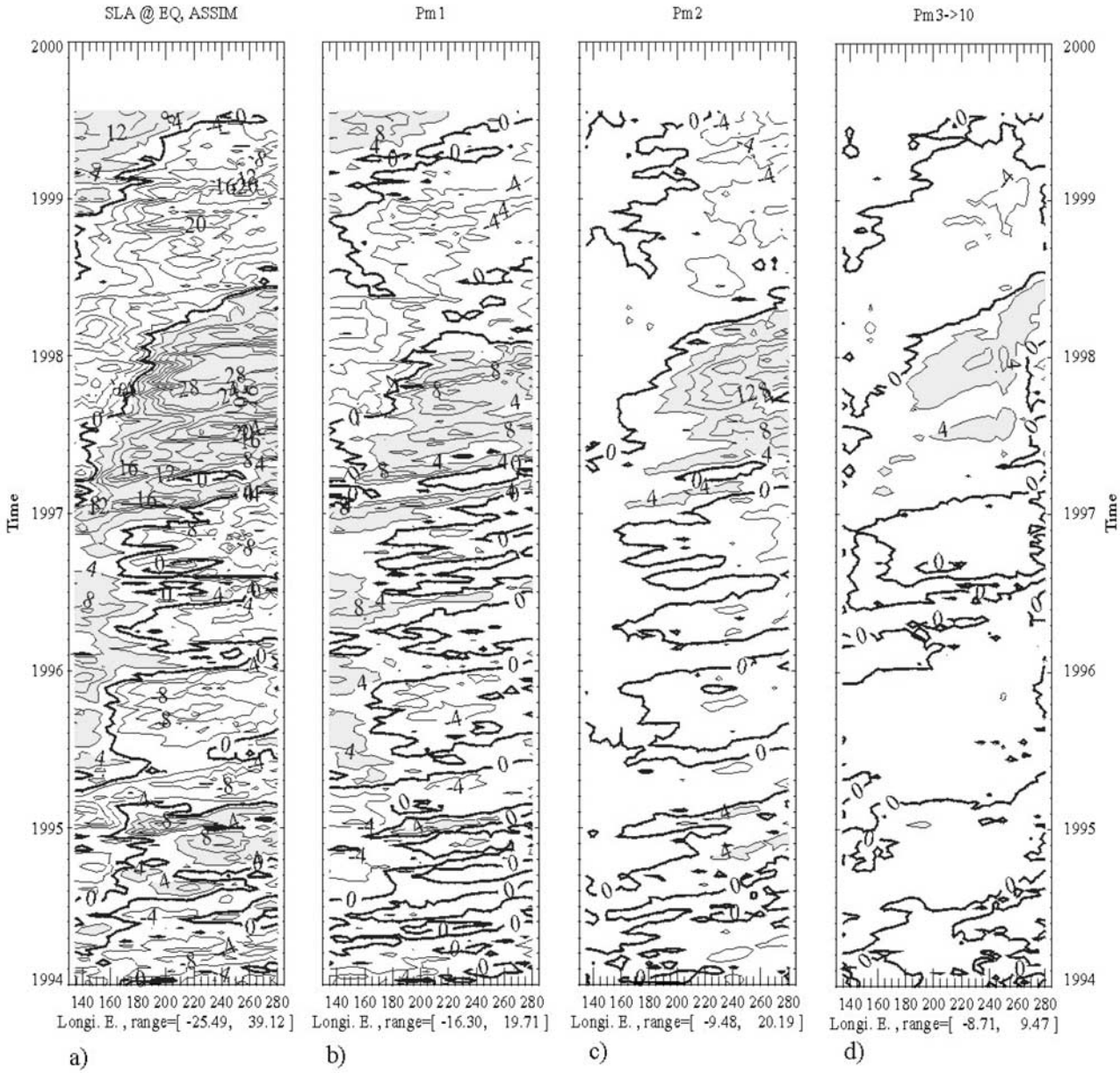

Figure 6. Time-longitude plots of (a) sea level anomalies (SLA) along the equator, and the contribution of (b) the first baroclinic mode, (c) the second one, and (d) the summed-up contribution of modes 3 to 10 from January 1994 until July 1999. Units are centimeters and contour intervals are every 4 cm. Shading is for anomalies larger than 4 cm.

the first two baroclinic modes. The Rossby contribution is displayed in reverse from 90°W to 140°E and the Kelvin contribution is repeated in order to visualize wave reflections at boundaries.

[34] In December 1996, a westerly wind anomaly event near the western boundary (Figure 11a) forces a first and second baroclinic mode downwelling Kelvin waves (Figures 9a and 10a). Their arrival at the NINO3 region corresponds to the end of cool conditions (Figure 11b). Later in March 1997, strong westerly wind anomalies force another couple of first and second baroclinic mode downwelling Kelvin waves which amplify the warming in the eastern Pacific. Note that the ratio of the Kelvin wave amplitude between the first and second baroclinic modes is 50% weaker for the March 1997 wind event than for the December 1996 wind event, suggesting a change in the meridional scale and location of the wind events. Note also that, whereas the first baroclinic mode Kelvin wave generally undergoes a decrease in amplitude as it propagates eastward, the second baroclinic mode Kelvin wave amplitude increases from about 140°W. These two waves eventually reflect at the eastern boundary at slightly different times because of differences in propagation speed.

[35] From mid-1997 onward, westerly wind anomalies develop near the date line in response to warmer SSTA in the eastern Pacific. In June–July 1997, wind anomalies around the dateline force strong downwelling Kelvin waves which induce strong eastward surface currents

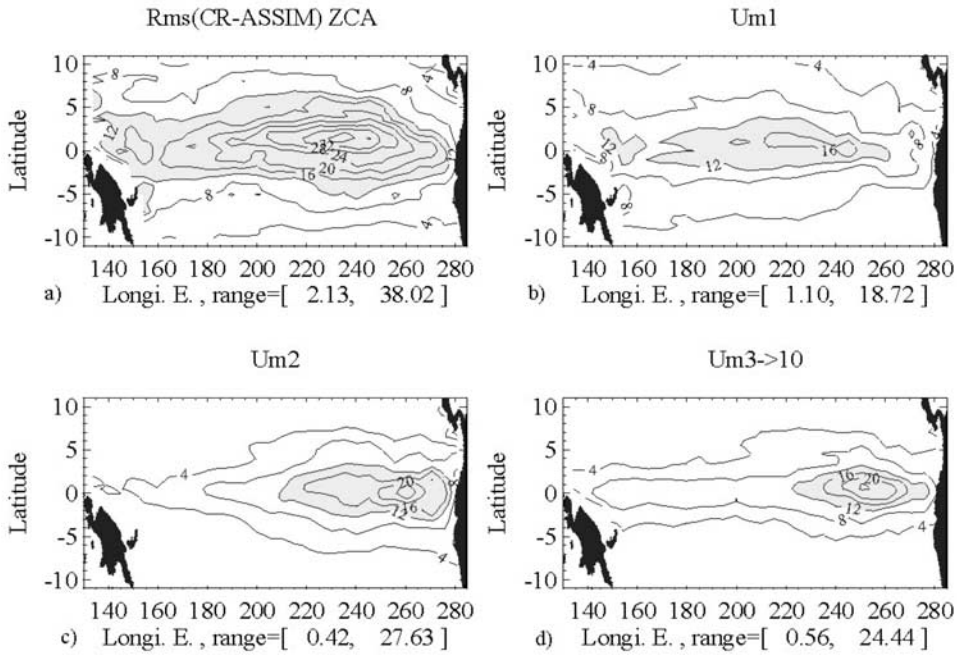

Figure 7. Maps of RMS difference between ASSIM and CR for (a) the total zonal current anomalies, and the contributions of (b) the first baroclinic mode, (c) the second baroclinic mode and (d) the sum of contributions of the third to the tenth mode. Units are cm s^{-1} and contour intervals are 4 cm s^{-1}. Shading is for value larger than 12 cm s^{-1}.

(Figure 5a). At the same time, easterly wind anomalies develop in the eastern Pacific. They act against the positive SLA induced by the first-meridional Rossby waves, resulting from the reflection of the downwelling Kelvin waves (see the negative anomalies in the summed-up contribution of mode 3 to 10 in the far eastern Pacific in the second half of 1997 in Figure 5d). On the other hand, these easterlies force anomalous westward currents (i.e., with the same sign than the ones induced by the same Rossby wave contribution). It is at this time that the reversal toward

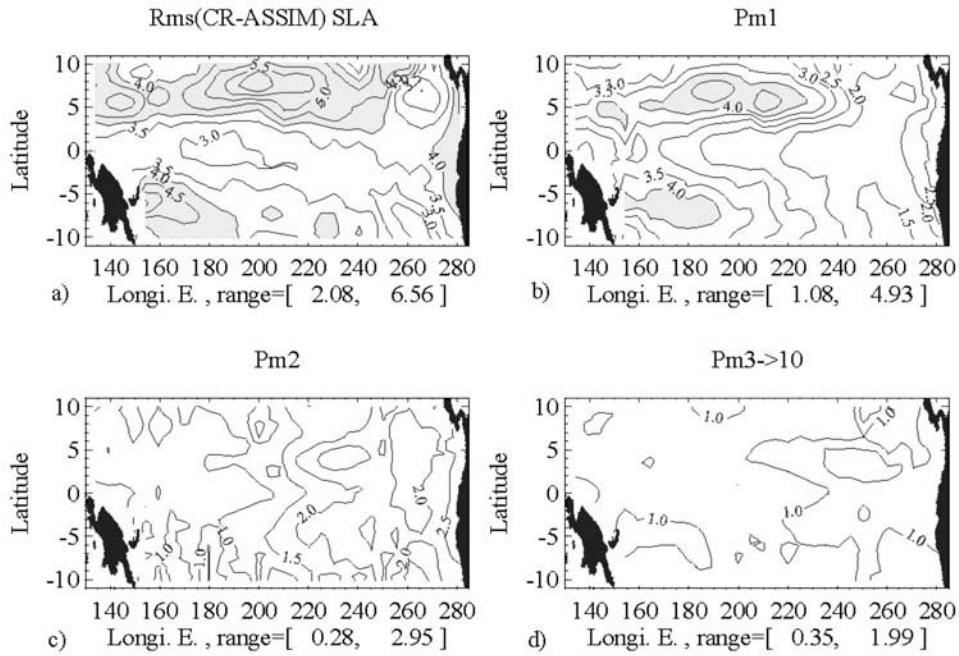

Figure 8. Same as Figure 7 but for sea level anomalies. Units are centimeters and contour intervals are 0.5 cm. Shading is for value larger than 4 cm.

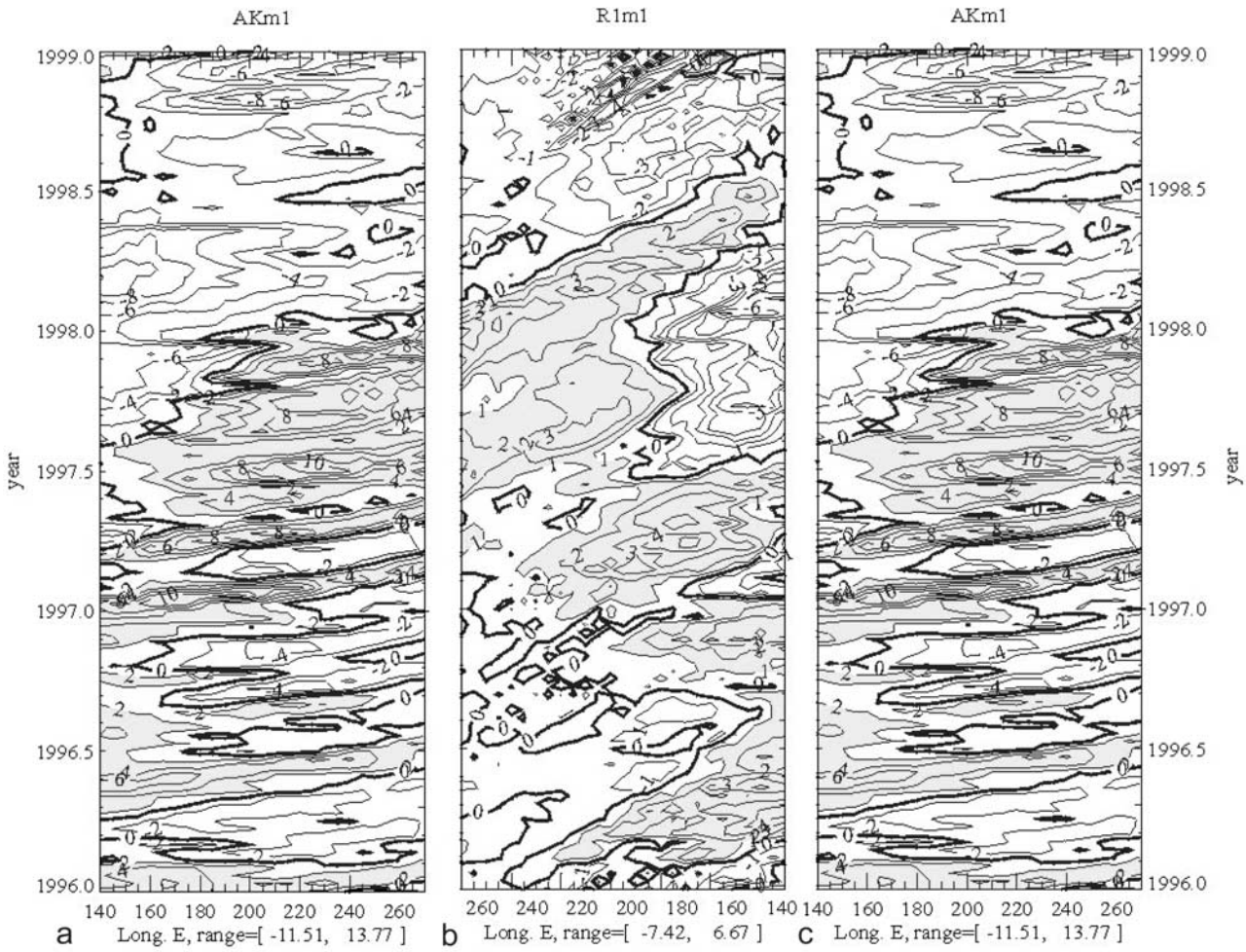

Figure 9. Longitude-time section of the (a) Kelvin (AK) and (b) first meridional Rossby mode (R1) contributions to sea level anomalies along the equator from January 1996 through January 1999 for the first baroclinic mode of ASSIM. R1 is displayed in reverse from 270°E to 140°E and (c) AK is repeated to visualize wave reflections at boundaries. Contour intervals are 2 cm for AK and 1 cm for R1. Shading is for anomalies larger than 2 cm (1 cm) for AK (R1). Note that linear theory predicts that, in the absence of modal dispersion, local wind-forcing and dissipation, the ratio of R1 (AK) versus AK (R1) should be ~1.22 (~0.44) near the eastern (western) boundary.

cooler conditions is initiated, according to the *Picaut et al.* [1997] mechanism which attributes to the anomalous westward currents the role of pushing back the warm pool to the west through zonal advection. The first three vertical modes contribute to these downwelling Rossby wave, but due to differences in wave speed, the first baroclinic mode Rossby wave extends farther west than the second and third baroclinic mode contribution, acting more constructively to the reversal toward cooler conditions at the mature stage of the cooling.

[36] In November 1997, the Rossby wave amplitude along the equator at 120°W is 1.5 cm (-7 cm s^{-1}), 4.0 cm (-10 cm s^{-1}) and 2.5 cm (-5 cm s^{-1}), respectively, for the first, second and third baroclinic mode contribution to SLAs (ZCAs). At that time, large westerly wind anomalies force strong downwelling Kelvin waves with a larger amplitude for the second baroclinic mode than for the first baroclinic one, because the wind variability has moved eastward. Starting in July 1997, the Kelvin waves amplitude for the second baroclinic mode increases along the wave path and at each pulses, whereas it decreases for the first baroclinic mode (see Figure 12). In December 1997, the second baroclinic mode contribution to sea level and zonal current anomalies is dominant in the eastern Pacific (Figures 5c and 6c). The second baroclinic mode Kelvin wave associated with the November 1997 wind event induces large westward anomalous currents through the reflected Rossby wave at the eastern boundary (see Figures 5c and 11b). Note the coherency between the Rossby wave amplitude and the 28°C isotherms in Figure 12 at that time. These conditions will last until June 1998 in the eastern Pacific for the second baroclinic mode, giving time for the zonal SST gradient to build up and to zonal advection to act onto SST changes. Note that in the eastern Pacific, there is a relatively weak contribution of the first baroclinic mode upwelling Kelvin waves in early 1998, compared to the second baroclinic Rossby wave contribution, suggesting that the mechanism at work for terminating the

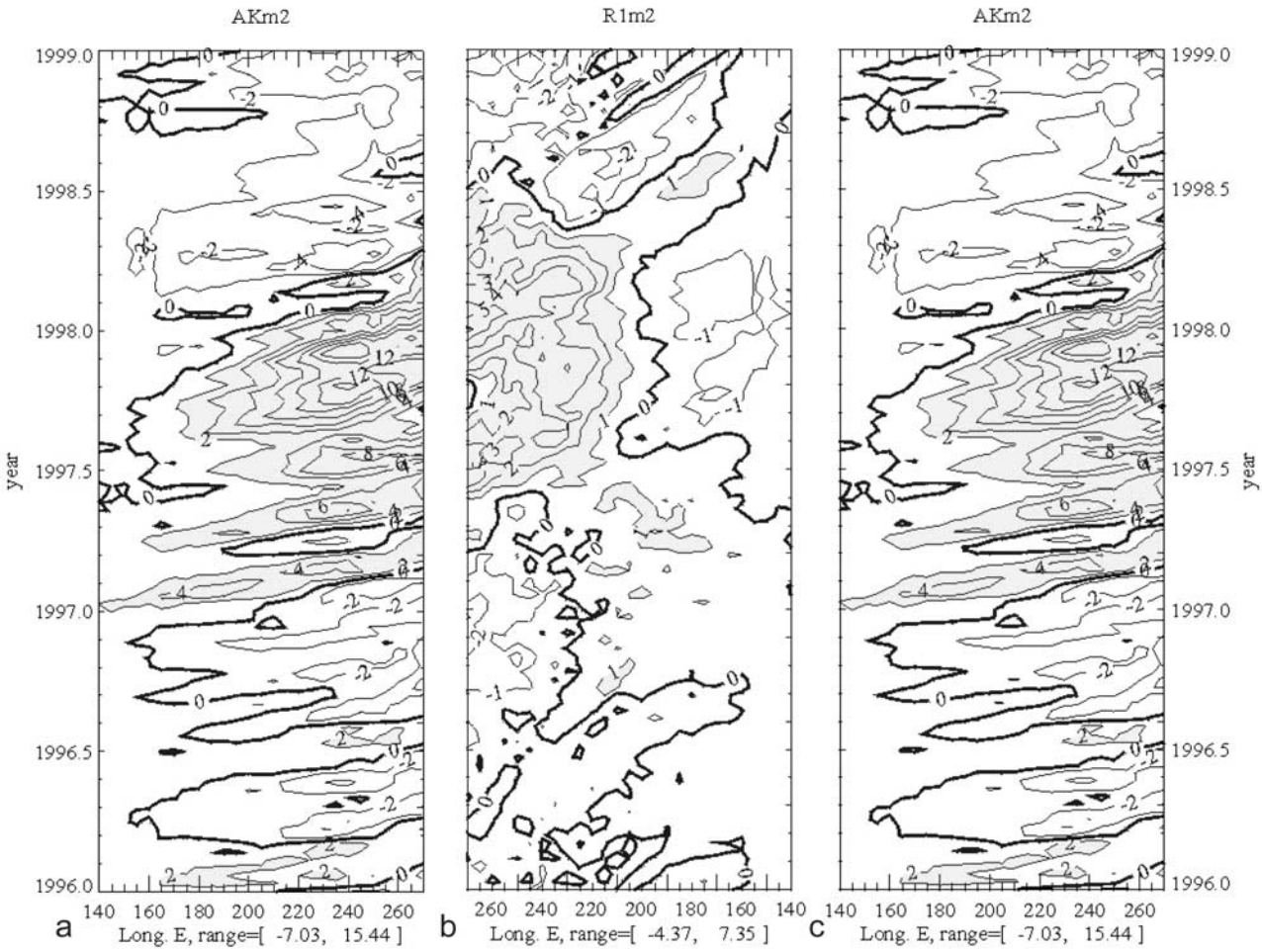

Figure 10. Same as Figure 9 but for the second baroclinic mode contribution.

1997–1998 El Niño may not involve the delayed action oscillator which attributes to the upwelling Kelvin wave reflected at the western boundary the reversal to the cold conditions.

5.2. Reflectivity on the Meridional Boundaries

[37] In order to complement the previous wave sequence description, an attempt is made to estimate the reflectivity power of the meridional boundaries for the long equatorial waves in ASSIM. To do so, the contribution of local wind-forcing to the waves is estimated from the outputs of a multimode simulation with the linear model parameter values for phase speed (c_n) and projection coefficient (P_n) derived from the vertical mode decomposition of ASSIM (compare Table 2 for parameter values at 150°W). The linear model is similar to the one used by *Dewitte et al.* [1999] except that a zonally varying projection coefficient ($P_n(x)$) was used. The model was forced with the ERS + TAO zonal and meridional wind stress anomalies as for ASSIM (heat flux is not considered) with a 5-day time step. Wave reflections were canceled at the meridional boundaries in order to consider only the contribution of the local wind-forcing to the wave contribution (i.e., there is no contribution of reflected waves). Kelvin (ak_m^{wind}) and n-meridional mode Rossby (rn_m^{wind}) coefficients for each baroclinic mode are derived in the same way as for ASSIM except that c_n does not vary with longitude (m denotes the baroclinic mode order and n the meridional mode number of the Rossby coefficient). Here c_n is taken at 150°W.

[38] The following quantities were then computed: Near the western boundary,

$$cw_{m,n}(x,t) = \frac{\left(ak_m - ak_m^{wind}\right)(x, t - \delta t_m(x))}{rn_m(x = 145°E, t)},$$

and near the eastern boundary,

$$ce_{m,n}(x,t) = \frac{\left(rn_m - rn_m^{wind}\right)(x, t + \delta t_m(x))}{ak_m(x = 90°W, t)},$$

where $\delta t_m(x)$ is the time needed for the waves to travel from 145°E (90°E) to the longitude x as a mth baroclinic mode Rossby (Kelvin) wave and then as a reflected mth-baroclinic mode Kelvin (Rossby) wave. ak_m and rn_m are the coefficients derived from ASSIM (see section 5.1). For the first(third)-meridional mode (n = 1(3)), linear theory predicts that for an infinite meridional wall: $cw_{m,n}$(x = 145°E,t) = 0.41 (0.13) and $ce_{m,n}$(x = 90°W,t) = 1.22 (0.94) [cf. *duPenhoat and Cane*, 1991]. These will be compared to those obtained from the model simulation. A least squares

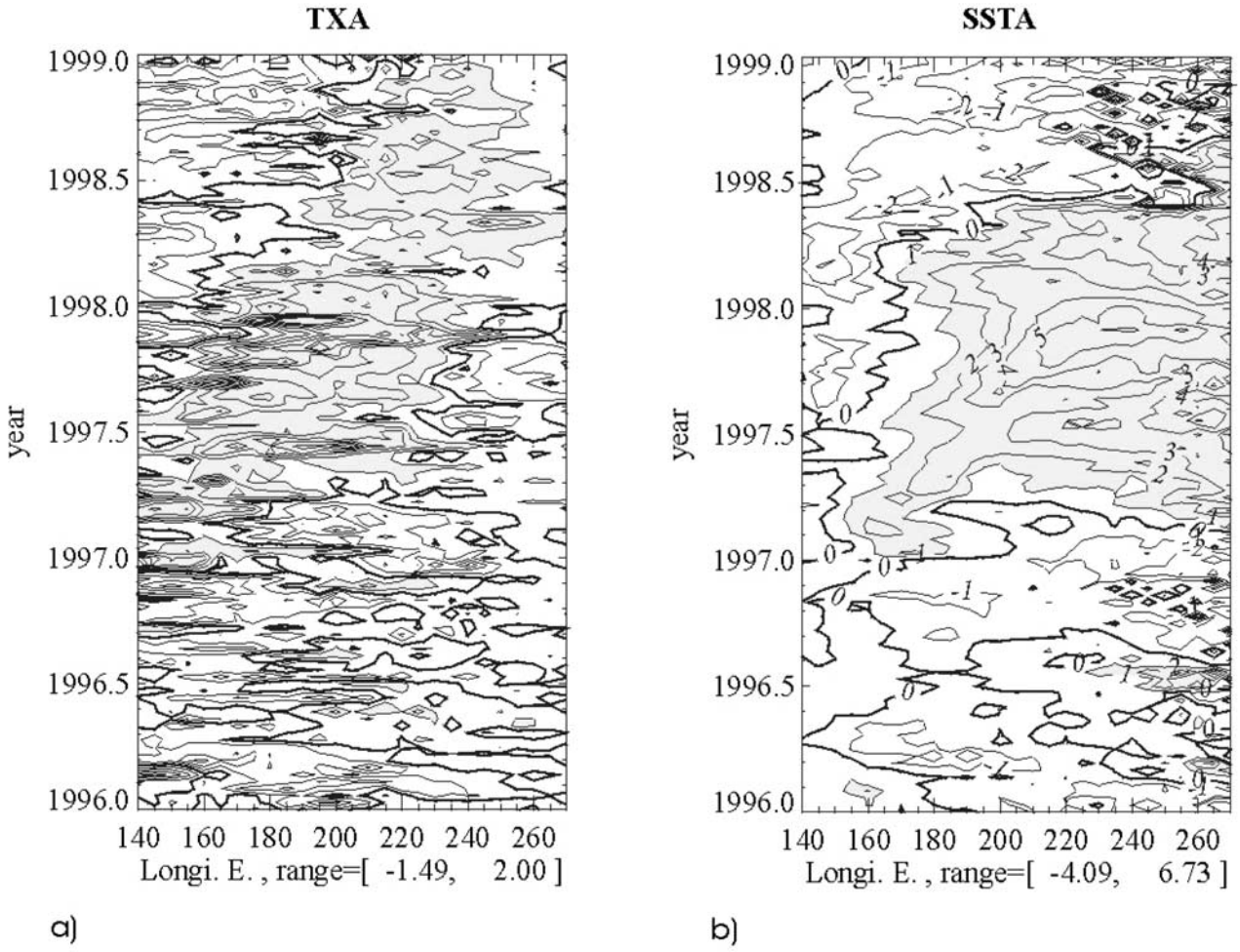

Figure 11. Longitude-time section of (a) zonal wind stress anomalies (ERS + TAO) in dyn cm^{-2} (contour intervals every 0.2 dyn cm^{-2}) and of (b) sea surface temperature anomalies from ASSIM in °C for the January 1996 through January1999 period. Shading is for anomalies larger than 0.2 dyn cm^{-2} (1°C) for zonal wind stress (temperature) anomalies.

linear fit was performed to the time series $cw_{m,n}(x, t)$ and $ce_{m,n}(x, t)$ to derive "average" coefficients ($\langle cw_{m,n}(x)\rangle$ and $\langle ce_{m,n}(x)\rangle$), and the reflection efficiency of the boundaries can be estimated (as a percentage of the reflection efficiency of an infinite meridional wall). Figure 13 displays the results for ASSIM for the first two baroclinic modes. Higher-order baroclinic modes are not considered because they are much less energetic and propagate very slowly so that the contributions of the reflected waves are small. Higher-order meridional modes are not considered either, for the same reasons.

[39] For the reflection at the eastern boundary, the results indicates that the American coast behaves almost as an infinite meridional wall for the long equatorial waves reflection, since values for $ce_{m,1}$ are close to the theoretical value from 90°W to 130°W for both baroclinic modes, and as far as 160°W for the first baroclinic mode. Note that we find for $ce_{m,2}$ a value close to zero (not shown) confirming that the American coast will not generate substantial antisymmetrical Rossby waves. The decrease of $ce_{2,1}$ west of 130°W may be due to an inaccurate estimation of the wind-forcing contribution to the Rossby wave coefficient since we use an empirical formulation for dissipation in the linear model. However, we expect from the higher-order baroclinic mode waves that they do not extend to the west as much as the first baroclinic mode waves since they are associated with the vertically propagating variability [cf. *Dewitte and Reverdin*, 2000]. Hence, from 130°W westward, one can consider that the eastern boundary is not "a reflector" of second baroclinic mode Kelvin waves.

[40] At the western boundary (~140°E), $cw_{m,1}$ is below the theoretical level by about 25% for both modes, suggesting a reflection efficiency of 75% of that of an infinite meridional wall. The $cw_{m,1}$ decreases slowly eastward leading to reflection efficiency of 45% at 170°W. For the second baroclinic mode, the reflection efficiency remains at an average level of 80% between 140°W and 150°W and then decreases sharply as the forced Kelvin waves are locally forced (compare Figure 9a). Note here that in the western Pacific, the second baroclinic mode contribution is much weaker than the first baroclinic mode contribution (compare section 4) so that a fair estimate of the actual reflection efficiency of the western boundary is given

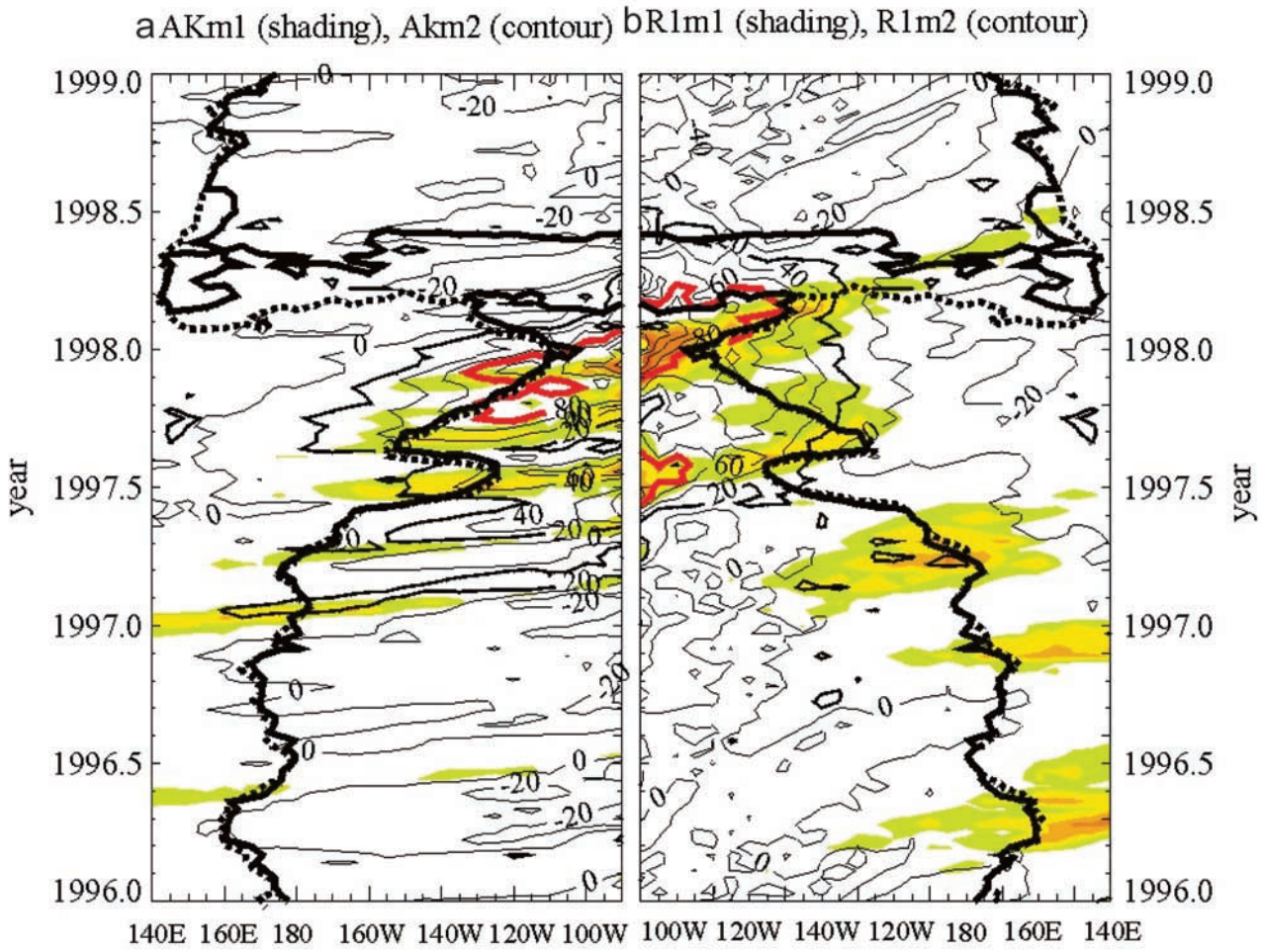

Figure 12. Longitude-time section of the (a) Kelvin and (b) first-meridional Rossby (displayed in reverse from 270°E to 140°E) mode contributions to zonal current anomalies along the equator from January 1996 through January 1999 for the first and second baroclinic modes. The shading (yellow scale) is for the first baroclinic mode Kelvin (first-meridional Rossby) wave amplitude whereas the contouring is for the second baroclinic mode Kelvin (first-meridional Rossby) wave amplitude. Contour intervals are 20 cm s^{-1}. The iso-line 80 cm s^{-1} is thicker and in red. The thick black dashed (dotted) line corresponds to the 28°C isotherm at 5 m (45 m). For the first baroclinic mode, only positive values are plotted.

(dominated) by $cw_{m,1}$, i.e., ~50% of an infinite meridional wall at ~165°E.

6. Discussion and Conclusions

[41] An OGCM simulation in which T/P + ERS data was assimilated is used to investigate the equatorial waves in the Pacific in 1994–1999. We first investigate the baroclinic mode contribution variability in the model simulations with and without assimilation of sea level data, which somehow provides a diagnosis of the impact of the assimilation of surface data and how the information is transmitted to the subsurface. Consistent with a lifting of the thermocline in the eastern part of the basin, the high-order baroclinic mode contribution is increased there. The assimilation also apparently increases the consistency between the sea surface temperature that should mimic the NCEP reanalysis through the heat flux "corrective" term and the dynamical fields. For instance, in the no-assimilation case, during the shift from warm to cold conditions (January–December 1998), the second baroclinic mode Rossby wave does not follow the 28°C isotherm as nicely as in the model simulation with assimilation (not shown), which indicates that the assimilation impacts the vertical structure in a physical (consistent) way. This also provides a different light for the interpretation of ENSO events in terms of long equatorial waves and their effects on SST. As an illustration, we present for the June 1997–June 1998 period (i.e., the period

Table 2. Linear Model Parameter Values

	c_n (in cm s^{-1})	P_n (adimensionalized)
Mode 1	2.75	0.56
Mode 2	1.65	0.41
Mode 3	1.00	0.12

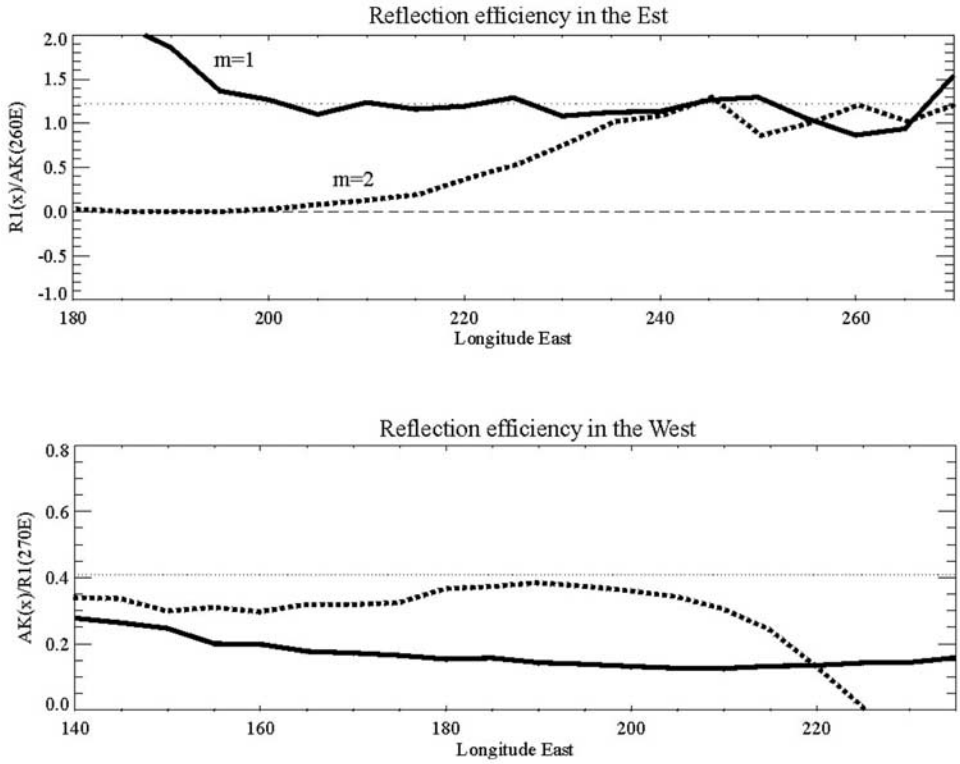

Figure 13. Reflection efficiency factor for Kelvin and first-meridional Rossby waves at the (top) eastern and (bottom) western boundaries for the two gravest baroclinic modes. The horizontal thin dotted line gives the theoretical level (i.e., when there is no local wind-forcing, dispersion or dissipation).

corresponding to the reversal toward cold conditions) an estimation of the first-meridional mode Rossby wave contribution to zonal advection of total temperature near the surface (i.e., $\frac{1}{60m}\int_0^{60m} Ur1_m(x,y,t)\frac{\partial T}{\partial x}(x,y,z,t)dz$, where $Ur1_m$ is the first-meridional Rossby mode contribution to zonal current anomalies for the mth baroclinic mode and T is the total temperature) for the first two baroclinic modes in ASSIM and CR (Figure 14). As expected, zonal advection of mean temperature by the anomalous zonal currents is the largest near the 28°C isotherm [*Picaut et al.*, 2001], namely in the eastern Pacific during the shift from warm to cold conditions. However, whereas there is relatively low coherency between the 28°C isotherm displacements and zonal advection in CR, zonal advection is concurrent with the position of the eastern edge of the warm pool in ASSIM. Also, the relative contribution of the baroclinic modes is changed between CR and ASSIM during this period. This, in particular, has clear consequences on the reflection efficiency of the meridional boundaries. Thus, the reflection efficiency of the first baroclinic mode at the eastern boundary is lower by ~50% in CR compared to ASSIM over the whole period (not shown). Caution is, however, required when interpreting such sensitivity considering the uncertainty on the method for deriving the reflection efficiency (in particular, the one related to the estimation of local wind-forcing contribution to the wave coefficients) and that the assimilation does not improve the model fields everywhere (see section 3).

[42] The wave coefficients for the gravest baroclinic modes from ASSIM are further investigated. For the Kelvin wave response, although the first two baroclinic modes are relatively highly correlated, they exhibit differences in their spatial distribution and amplitude evolution both as the waves propagate and as warm conditions develop. In particular, for the three consecutive strong wind events (January 1997, March 1997 and June 1997), the associated second baroclinic mode Kelvin wave amplitude increases as the waves propagate eastward whereas the first baroclinic mode Kelvin wave has a maximum amplitude near the wind-forcing region, i.e., in the western and central parts of the basin. Also, as the warm conditions develop, the second baroclinic Kelvin waves amplitude increases reaching 15 cm in November 1997 (compared to ~7 cm in June 1997), whereas the one of the first baroclinic mode Kelvin wave decreases to ~8 cm in November 1997 (compared to ~12 cm in June 1997). Note that the projection is performed considering a mean density structure, although the thermocline is depressed during the mature phase of El Niño, which modifies the vertical mode functions. This, in particular, leads to an "overestimation" by ~15% of the second baroclinic mode Kelvin wave amplitude as compared to a calculation that takes into account the instantaneous profiles. Whether or not these characteristics of the Kelvin waves are due to modal dispersion processes [*Busalacchi and Cane*, 1988] or to changes in the wind-forcing characteristics needs to be clarified.

[43] The Rossby wave response varies also according to the baroclinic modes. As expected, the westward propagation of the waves is clearer for mode 1 than for mode 2, since the higher-order modes dissipate faster than the

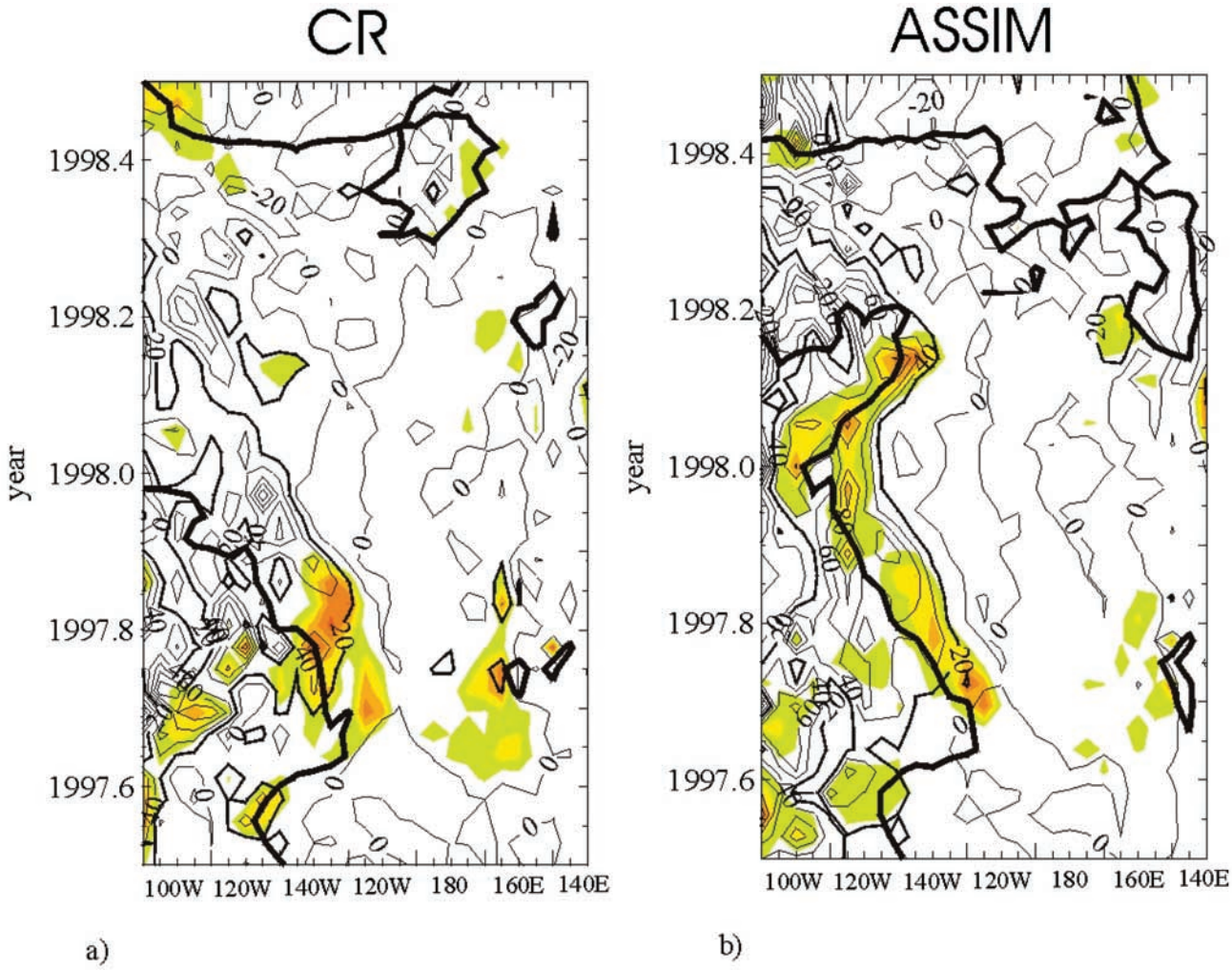

Figure 14. Longitude-time section (displayed in reverse from 90°W to 140°E) of the first-meridional Rossby mode contributions to zonal advection of mean temperature for the (yellow scale) first and (contour) second baroclinic modes along the equator from June 1997 through June 1998 for (a) CR and (b) ASSIM. Contour intervals are every 20 units. Units are 10^{-5} °C s^{-1}. The iso-line 20 unit is thicker. The thick solid line corresponds to the 28°C isotherm at 5 m. The shading is for positive value (i.e., westward anomalous currents). For the first baroclinic mode, only positive values are plotted.

gravest mode. In particular, the reflected Rossby wave at the eastern boundary of the first baroclinic wave extends farther west than the one of the second baroclinic mode. Unlike the Kelvin wave response, as the warm conditions settle down, the Rossby wave amplitude of both the first and second baroclinic modes increases.

[44] The reflection efficiency of the zonal boundaries was estimated for the first two baroclinic modes. A ~100% level is found close to the eastern boundary for both modes. Farther from the American coast, west of 130°W, the reflection efficiency decreases to ~50% due to dissipation (i.e., vertical propagation of the higher-order modes). At the western boundary, we found 70% for the first baroclinic mode and 80% for the second baroclinic mode. However, for the first baroclinic mode, it decreases to less than 50% at 160°E, which, relative to the energy of the baroclinic modes, results in an actual ~50% reflection efficiency near 165°E since the second baroclinic mode is much weaker than the first baroclinic mode in the western Pacific. It is interesting to note that for both modes, the reflection efficiency is of the same order of magnitude close to the zonal boundaries (slightly lower for mode 1 than for mode 2 at the western boundary), which may explain in part why an estimate from the "one mode" approximation [cf. *Boulanger and Menkes*, 1999] provides a realistic value. However, at the western boundary, our estimate of reflection efficiency is lower than those of *Boulanger and Fu* [1996] and *Boulanger and Menkes* [1999] who found that the reflection of the first-meridional Rossby wave does explain more than 90% of the Kelvin wave variance. On the other hand, at the eastern boundary, our estimate is larger than the ~75% reflection efficiency that they found for the Kelvin waves reflecting into a first meridional Rossby wave. These differences are believed to be due to the taking into consideration of the vertical structure of the ocean. The vertical mode decomposition is required to represent the

wave propagations of the gravest modes taking into account the differences in phase speed and meridional structures. It is also required to separate the variability which actually propagates from the part which is quasistationary and mostly associated with the slower higher-order baroclinic modes. In our calculation, we also remove an estimation of the local wind-forcing contribution to the reflected wave, obtained from a linear model simulation. This is actually the biggest limitation of our calculation since a linear dissipation is used in the model [cf. *Dewitte et al.*, 1999], which may be oversimplified. Note however that in a multimode context, the linear dissipation is suitable for explaining the processes of vertical propagation responsible for the decay of the wave amplitude at the surface [*Dewitte and Reverdin*, 2000]. Also, the variability of the mixed layer depth was not taken into account. This, as well as nonlinearities, may impact the transmission of momentum into the baroclinic ocean, and thus our estimation of the wind-forcing. Sensitivity tests to the projection coefficient of the wind, P_n, (taken with and without longitudinal dependency) suggests, however, that such impact should be weak.

[45] In light of the results of the vertical mode decomposition, it is now interesting to document some aspects of the potential theories for ENSO that are the delayed oscillator theory [*Schopf and Suarez*, 1988; *Battisti*, 1988] and the zonal advection feedback theory recently suggested by *Picaut et al.* [1997]. These theories attribute to vertical advection (western boundary reflection) and zonal advection (eastern boundary reflection), respectively, the main role in the development (termination) of a warm event. The results reported here suggest that both mechanisms are at work in the simulation and that the vertical structure determines the relative impact of them on SST changes: The December 1996 and March 1997 events did produce strong westward anomalous currents that projected largely onto the higher-order modes (compare Figure 5d), as well as a deepening of the thermocline a few months later in the eastern Pacific mostly associated with the gravest baroclinic mode contributions (compare Figures 6b and 6c). The formers induced zonal advection of mean temperature since the thermal front of the warm pool was well defined at that time, whereas the latter induced vertical advection of mean temperature since the thermocline is relatively shallow before the warming. Note that reflections of Rossby waves at the western boundary partially contribute to the Kelvin waves of the first baroclinic mode (compare Figures 9b and 9c). This is less the case for the second baroclinic mode Kelvin wave, which is mostly forced by the wind. As the eastern edge of the warm pool starts moving eastward, there is an increased contribution of the second baroclinic mode. The 28°C isotherm reaches the eastern boundary in December 1997 at the time when the last wind forced strong Kelvin waves reflect at the eastern boundary as first meridional Rossby waves. The Rossby waves of both vertical modes initiated the reversal of the displacement of the eastern edge of the warm pool through zonal advection (see Figures 12 and 14b). The first baroclinic mode Rossby wave is however less efficient in pushing back the 28°C isotherms westward than the second baroclinic mode Rossby wave at the beginning of the cooling (see the thick black solid and dashed lines mimicking the thick red line in January, February and March 1998 on Figure 12b). A pool of surface warm water (see the difference on Figure 12 between the 28°C isotherm at the surface and at 45 m) remains in the far eastern Pacific until May 1998. On the contrary, the 28°C isotherm at 45 m follows perfectly the 60 cm s^{-1} isoline of the second baroclinic mode as far as 130°W. The front at this depth is dragged farther westward as far as 170°W by the first baroclinic mode wave, suggesting that the zonal advection of mean temperature takes place just below the surface. Results of Figure 14b, which presents the vertically integrated zonal advection of mean temperature associated with the first-meridional Rossby wave, corroborate such observations. Thus the abrupt shift toward cooler conditions is apparently first associated with the second baroclinic mode Rossby wave which induces zonal advection of mean temperature just below the surface in the eastern Pacific and then relayed by the first baroclinic Rossby wave in the central and eastern Pacific. By March 1998 a second baroclinic mode upwelling Kelvin wave, apparently forced by easterlies developing in the far western Pacific, develops east of 150°W (compare isoline −20 cm s^{-1} (−2 cm) on Figure 12a (10a)) and also participates in the cooling at the surface.

[46] To summarize, we find that both baroclinic modes could contribute through zonal and vertical advection to the development of the warm conditions during the 1997–1998 El Niño. The mature phase of the event is concurrent with an increased contribution of the second baroclinic mode which becomes dominant over the first baroclinic mode. The termination mechanism of this event fits the one proposed by *Picaut et al.* [1997], namely that the reversal toward cooler conditions is associated with the Rossby waves reflected at the eastern boundary. Both modes contributed constructively to the westward displacement of the 28°C isotherm at the surface with however a privileged role of the second baroclinic mode in initiating the reversal. There is no clear evidence of reflected upwelling Kelvin signal for explaining the cooling. A second baroclinic upwelling Kelvin wave did contribute to the return to normal condition at the sea surface, but it appears to be mostly forced by easterlies at the western boundary. As pointed out by *Picaut et al.* [2002], there is however not only one mechanism at work during the development and termination of the 1997–1998. In order to clarify the relative importance of the delayed oscillator and zonal advective feedbacks onto SST changes among all the other potential mechanisms involved (see *Wang* [2001] for a review), further investigation based on the estimation of the Kelvin and Rossby wave contributions to the advection terms is needed. This study suggests that the peculiarity of the baroclinic modes will have to be taken into account, which could be done as more and more reliable assimilation products become available.

[47] **Acknowledgments.** The XBT data were kindly provided by Neville Smith from BMRC. We also thank AVISO for the altimetric data. This paper benefited from fruitful discussions with Gilles Reverdin. The two anonymous reviewers are thanked for their constructive comments.

References

Battisti, D. S., Dynamics and thermodynamics of a warming event in a coupled tropical atmosphere-ocean model, *J. Atmos. Sci.*, *45*, 2889–2919, 1988.

Blanke, B., and P. Delecluse, Variability of the tropical Atlantic ocean simulated by a general circulation model with two different mixed layer physics, *J. Phys. Oceanogr.*, *23*, 1363–1388, 1993.

Boulanger, J.-P., and L.-L. Fu, Evidence of boundary reflection of Kelvin and first-mode Rossby waves from TOPEX/POSEIDON sea level data, *J. Geophys. Res.*, *101*, 16,361–16,371, 1996.

Boulanger, J.-P., and C. Menkes, Long equatorial waves reflection in the Pacific ocean from Topex/Poseidon data during the 1992–1998 period, *Clim. Dyn.*, *15*, 205–225, 1999.

Busalacchi, A. J., and M. A. Cane, The effect of varying stratification on low-frequency equatorial motions, *J. Phys. Oceanogr.*, *18*, 801–812, 1988.

Cane, M. A., A. Kaplan, R. N. Miller, B. Tang, E. C. Hackert, and A. J. Busalacchi, Mapping tropical Pacific sea level: Data assimilation via a reduced state Kalman filter, *J. Geophys. Res.*, *101*, 22,599–22,617, 1996.

Delcroix, T., B. Dewitte, Y. duPenhoat, F. Masia, and J. Picaut, Equatorial waves and warm pool displacement during the 1992–1998 El Niño events, *J. Geophys. Res.*, *105*, 26,045–26,062, 2000.

Dewitte, B., Sensitivity of an intermediate ocean-atmosphere coupled model of the tropical Pacific to its oceanic vertical structure, *J. Clim.*, *13*, 2363–2388, 2000.

Dewitte, B., and G. Reverdin, Vertically propagating annual and interannual variability in an OGCM simulation of the tropical Pacific ocean in 1985–1994, *J. Phys. Oceanogr.*, *30*, 1562–1581, 2000.

Dewitte, B., G. Reverdin, and C. Maes, Vertical structure of an OGCM forced simulation of the tropical Pacific in 1985–1994, *J. Phys. Oceanogr.*, *29*, 1542–1570, 1999.

Dewitte, B., D. Gushchina, Y. duPenhoat, and S. Lakeev, On the importance of subsurface variability for ENSO simulation and prediction with intermediate coupled models of the Tropical Pacific: A case study for the 1997–1998 El Niño, *Geophys. Res. Lett.*, *29*(14), 1666, doi:10.1029/2001GL014452, 2002.

Ducet, N., P. Y. Le Traon, and G. Reverdin, Global high resolution mapping of ocean circulation from TOPEX/POSEIDON and ERS-1/2, *J. Geophys. Res.*, *105*, 19,477–19,498, 2000.

duPenhoat, Y., and M. A. Cane, Effects of low-latitude western boundary gaps on the reflection of equatorial motions, *J. Geophys. Res.*, *96*, 3307–3322, 1991.

Fu, L.-L., E. J. Christensen, C. A. Yamarone Jr., M. Lefebvre, Y. Menard, M. Dorrer, and P. Escudier, Topex/Poseidon mission overview, *J. Geophys. Res.*, *99*, 24,369–24,381, 1994.

Fukumori, I., R. Raghunath, L. L. Fu, and Y. Chao, Assimilation of RTOPEX/Poseidon altimeter data into a global ocean circulation model: How good are the results?, *J. Geophys. Res.*, *104*, 25,647–25,665, 1999.

Gent, P. R., and M. A. Cane, A reduced gravity primitive equation model of the upper equatorial ocean, *J. Comput. Phys.*, *81*, 444–480, 1989.

Gourdeau, L., J. Verron, T. Delcroix, R. Murtugudde, and A. J. Busalacchi, Assimilation of Topex/Poseidon altimetric data in a primitive equation model of the tropical Pacific Ocean during the 1992–1996 ENSO period, *J. Geophys. Res.*, *105*, 8473–8488, 2000.

Hayes, S. P., P. Chang, and M. J. McPhaden, Variability of the sea surface temperature in the eastern equatorial Pacific during 1986–1988, *J. Geophys. Res.*, *96*, 10,553–10,566, 1991.

Jin, F. F., An equatorial ocean recharge paradigm for ENSO: I. Conceptual model, *J. Atmos. Sci.*, *54*, 811–829, 1997.

Kalnay, E., et al., The NCEP/NCAR Reanalysis Project, *Bull. Am. Meteorol. Soc.*, *77*, 437–471, 1996.

Kessler, W. S., and J. P. McCreary, The annual wind-driven Rossby wave in the subthermocline equatorial Pacific, *J. Phys. Oceanogr.*, *23*, 1192–1207, 1993.

Le Traon, P. Y., and F. Ogor, ERS-1/2 orbit improvement using TOPEX/Poseidon: The 2-cm challenge, *J. Geophys. Res.*, *103*, 8045–8057, 1998.

Madec, G., P. Delecluse, M. Imbard, and C. Levy, OPA 8.1 Ocean General Circulation Model reference manual, *Nodes du pole de model. 11*, 91 pp., Inst. Pierre Simon Laplace, Paris, 1999.

McPhaden, M., Genesis and evolution of the 1997–98 El-Niño, *Science*, *283*, 950–954, 1999.

McPhaden, M. J., et al., The Tropical Ocean Global Atmosphere (TOGA) observing system: A decade of progress, *J. Geophys. Res.*, *103*, 14,169–14,240, 1998.

Menkes, C., et al., Impact of TAO vs. ERS wind stresses onto simulations of the tropical Pacific Ocean during the 1993–1998 period by the OPA OGCM, in *Climate Impact of Scale Interactions for the Tropical Ocean-Atmosphere System*, *Euroclivar Workshop Rep. 13*, pp. 46–48, World Clim. Res. Programme, Geneva, 1998.

Parent, L., Assimilation de données dans l'océan Pacifique tropical sur la période 1994–1998, Ph. D. thesis, 222 pp., Univ. Joseph Fourier, Grenoble, France, 2000.

Parent, L., C.-E. Testut, J.-M. Brankart, J. Verron, P. Brasseur, and L. Gourdeau, Assimilation of Topex/Poseidon and ERS altimetric data in the tropical Pacific Ocean during 1994–1998: The use of TAO data to reference mean sea-surface height, *J. Mar. Res.*, in press, 2002.

Pham, D. T., J. Verron, and M. C. Roubaud, A singular evolutive extended Kalman filter for data assimilation in oceanography, *J. Mar. Syst.*, *16*, 323–340, 1998.

Picaut, J., F. Masia, and Y. DuPenhoat, An advective-reflective conceptual model for the oscillatory nature of ENSO, *Science*, *277*, 663–666, 1997.

Picaut, J., M. Ioualalen, T. Delcroix, F. Masia, R. Murtugudde, and J. Vialard, The oceanic zone of convergence on the eastern edge of the Pacific warm pool: A synthesis of results and implications for El Niño-Southern Oscillation and biogeochemical phenomena, *J. Geophys. Res.*, *106*, 2363–2386, 2001.

Picaut, J., E. Hackert, A. J. Busalacchi, R. Murtugudde, and G. S. E. Lagerloef, Mechanisms of the 1997–1998 El Niño-La Niña, as inferred from space-based observations, *J. Geophys. Res.*, *107*(C5), 3037, doi:10.1029/2001JC000850, 2002.

Radenac, M.-H., C. Menkes, J. Vialard, C. Moulin, Y. Dandonneau, T. Delcroix, C. Dupouy, A. Stoens, and P.-Y. Deschamps, Impacts of dynamics on Nitrate and new production in the equatorial Pacific during the 1997–98 El Niño: A synthesis from models and observations, *J. Geophys. Res.*, *106*, 26,879–26,889, 2001.

Reynolds, R. W., and T. M. Smith, Improved global sea surface temperature analyses using optimum interpolation, *J. Clim.*, *7*, 929–948, 1994.

Schopf, P. S., and M. J. Suarez, Vacillations in a coupled ocean-atmosphere model, *J. Atmos. Sci.*, *45*, 549–566, 1988.

Shu, L., and A. J. Clarke, Using an ocean model to examine ENSO dynamics, *J. Phys. Oceanogr.*, *32*, 903–923, 2002.

Smith, N. R., An improved system for tropical ocean sub-surface temperature analysis, *J. Atmos. Oceanic Technol.*, *12*, 850–870, 1995.

Verron, J., L. Gourdeau, D. T. Pham, R. Murtugudde, and A. J. Busalacchi, An extended Kalman filter to assimilate satellite altimeter data into a nonlinear numerical model of the tropical Pacific Ocean: Method and validation, *J. Geophys. Res.*, *104*, 5441–5458, 1999.

Vialard, J., and P. Delecluse, An OGCM study for the TOGA decade: I. Role of salinity in the physics of the western Pacific fresh pool, *J. Phys. Oceanogr.*, *28*, 1071–1088, 1998a.

Vialard, J., and P. Delecluse, An OGCM study for the TOGA decade: II. Barrier layer formation and variability, *J. Phys. Oceanogr.*, *28*, 1089–1106, 1998b.

Vialard, J., C. Menkes, J. P. Boulanger, P. Delecluse, E. Guilyardi, and M. J. McPhaden, Oceanic mechanisms driving the SST during the 1997–1998 El Niño, *J. Phys. Oceanogr.*, *31*, 1649–1675, 2001.

Wang, C., On the ENSO mechanisms, *Adv. Atmos. Sci.*, *18*, 674–691, 2001.

Yeh, S.-W., B. Dewitte, J.-G. Jhun, and I.-S. Kang, The characteristic oscillation induced by coupled processes between oceanic vertical modes and atmospheric modes in the tropical Pacific, *Geophys. Res. Lett.*, *28*, 2847–2850, 2001.

B. Dewitte, IRD/UR065/LEGOS, B.P. A5, 98848 Nouméa, New Caledonia.

Y. duPenhoat, L. Gourdeau, and S. Illig, Laboratoire d'Etudes en Géophysique et Océanographie Spatiales, CNES/IRD, Toulouse, France.

L. Parent and J. Verron, Laboratoire des Ecoulements Géophysique et Industriels, UMR5519/CNRS/UJF/INPG, Grenoble, France.